Special Issue: Aeroacoustics and non-linear structural dynamics in Turbomachines

Near-and-far field modeling of advanced tail-rotor noise using source-mode expansions

Michel Roger [a,*], Korcan Kucukcoskun [b]

[a] *LMFA, UMR CNRS 5509, 36 Avenue Guy de Collongue, Univ. Lyon, École Centrale de Lyon, Écully, 69134, France*
[b] *Siemens PLM Software, Belgium*

ARTICLE INFO

ABSTRACT

The present work is aimed at illustrating a hybrid analytical/numerical methodology that could be used at the early-design stage to predict the tonal noise of an axial-flow fan surrounded by solid surfaces. A model shrouded helicopter tail-rotor architecture is selected as a typical example of unconventional rotor-stator stage. The advanced design involves uneven rotor-blade spacing and leant stator vanes, one of which is replaced by the transmission shaft. Both the rotor and the stator generate tonal noise at the same frequencies, because of the potential distortion around the shaft and because of the impingement of the blade wakes on the vanes, respectively. Source-modes made of circular distributions of stationary sources properly phase-shifted are introduced to reproduce all sources in a unified way, based on analytical expressions. This part is based on simplified unsteady aerodynamic theories. The source-modes are then used as input in a numerical software solving the Helmholtz equation to assess the sound scattering by the shroud. The approach is applied only to the stator noise for illustration and typical results are discussed.

© 2019 Elsevier Ltd. All rights reserved.

1. Introduction

Analytical modeling of the aerodynamic sound radiated from rotor-stator stages is a topic of major engineering interest at the time of preliminary design of a turbomachine. In many situations the stage is operating in close vicinity of other stationary bodies or solid surfaces, some of which directly contribute to the sound generation whereas some other act as diffracting obstacles. The latter are thus referred to as passive surfaces and the former as active surfaces. Both must be clearly identified when looking for low-noise design rules. Typically the aerodynamic interactions between the rotating blades and the stationary vanes or other close obstacles such as supporting struts directly produce sound but have a moderate effect on sound propagation (at least for small-size struts and non-overlapping blades/vanes). In contrast the surface of a casing redistributes the radiated sound but does not significantly produce additional noise. Reduction at source is a strategy for which *a priori* only the active surfaces need to be considered. Yet this is not enough for a reliable estimate of the radiated sound as perceived by a far-field observer. This suggests that the modeling effort must include two steps, namely the description of the sources and of their direct free-field sound radiation, on the one hand, and the quantification of the major diffracting effects caused by passive surfaces, on the other hand. The present work is aimed at associating an analytical source model and a numerical diffraction model in order to demonstrate this need. It addresses the shrouded tail rotor of a helicopter as a typical example but the same approach could be applied to many other configurations of rotating blade technology.

---

* Corresponding author.
  E-mail address: michel.roger@ec-lyon.fr (M. Roger).

Nomenclature

$a = a_R + ia_I$	model potential-distortion harmonic
a_c	shaft cross-section radius
A_s	phase factor in the definition of F_s
b	half wake width
B	blade number (rotor)
c	chord length
c_0	sound speed
d	rotor-stator interaction distance
e_X, e_Y, e_Z	unit vectors of main directions
E	complex Fresnel integral
F	point-dipole force
F$_s$	point-dipole force harmonic
F_s	blade/vane loading harmonic
G	free-space Green's function
I_N, I_s	interference sums (heterogeneous rotor)
K	modified wavenumber in potential-interaction model
k, k_{mB}, k_s	acoustic wavenumbers for $\omega, mB\Omega/c_0, s\Omega/c_0$
k_1, k_2	chordwise and spanwise aerodynamic wavenumbers
k_1^*, k_2^*	dimensionless aerodynamic wavenumbers
k_d	damping factor in potential-interaction model
L	vane-span length
$\ell_s(y_1), \widetilde{\ell}_s(y_1,y_2)$	local harmonic lift on a blade/vane
$\ell'(r)$	spanwise hub-distance of a leant-vane point
$M = \Omega r/c_0$	tangential Mach number
M_0	convection Mach number U/c_0
M_t	blade-tip Mach number
m	BPF harmonic order
n	spinning-mode order (number of lobes)
N	shaft-rotation harmonic order
p_{mB}	complex acoustic pressure at a BPF harmonic
r	radial polar coordinate of a source point
R	observer distance to origin (spherical coordinate)
R'	observer distance to a source point
R_α	observer distance to a source-mode point
r_H, r_T	hub and tip radii
s	blade/vane loading harmonic order
U	convection speed over a blade or vane

U_t	spanwise trace speed
V	vane number (stator)
V_r	absolute mean-flow velocity at rotor exit
W	relative mean-flow velocity at rotor exit
w	relative velocity deficit in a blade wake
w_s	velocity-distortion harmonic (wake or potential distortion)
w_d	maximum velocity deficit in a blade wake
x	observer coordinate vector
x	distance from trailing edge along wake centerline
X	observer coordinate along the downstream shaft axis
Y	vertical observer coordinate
y_1, y_2, y_3	chordwise, spanwise and normal coordinates in blade/vane reference frame
y_1^*	dimensionless chordwise coordinate $2y_1/c$
Z	observer coordinate along the rotor axis
α	polar angle of source-mode point
α_j	angular blade displacement in a heterogeneous rotor
$\beta = \sqrt{1 - M^2}$	compressibility parameter
γ	rotor-blade stagger angle
γ'	stator-vane stagger angle
ζ	vane lean-angle
κ, κ'	modified dimensionless wavenumbers
μ, μ_s	dimensionless frequency parameters in unsteady aerodynamic models
ξ	ln2
θ	observer angle from axis (spherical coordinate)
φ	observer angle around axis (spherical coordinate)
Φ	complex error function
$\psi(r)$	angular deviation of a leant-vane point
τ	half wake-passage time on a vane
ω	angular frequency
Ω	rotor rotational speed
Ω_s	angular phase speed of a spinning mode
BPF	blade passing frequency
BLH	blade loading harmonic
FEM	Finite Element Method
PIN	potential-interaction noise
WIN	wake-interaction noise

A typical advanced shrouded tail rotor is depicted in Fig. 1. The view from downstream shows the radial transmission shaft aligned with the forward-flight direction and the stator vanes, both as black surfaces, whereas the view from inlet clearly shows the rotor blades. From the aerodynamic standpoint a higher efficiency is reached with the shrouded tail-rotor than with a more conventional isolated rotor because of the swirl recovery achieved by the stator. In forward flight the fin also produces the necessary anti-torque force. Furthermore the casing ensures protection for a safer operability. In Fig. 1 low-noise design concepts addressed in following sections and implemented on modern helicopters are also illustrated. The first one consists in resorting to leant vanes instead of radial vanes (left-side view); the second one consists in introducing uneven blade-to-blade angular spacing (right-side view). The transmission shaft is another important specific feature. It causes localized flow obstruction, on the one hand, and takes a place that would be that of a stator vane in a complete stator, on the other hand. The resulting heterogeneity in the blade and vane distributions makes the tail rotor a typical example of unconventional rotor-stator stage, if conventional or homogeneous stages are defined by rotors (stators) with identical and periodically distributed blades (vanes).

Deviations from homogeneity are numerous in rotating-blade technology. For instance the design of modern car-engine cooling units involves similar features. Indeed the fan itself, possibly with uneven blade spacing, is associated with a set
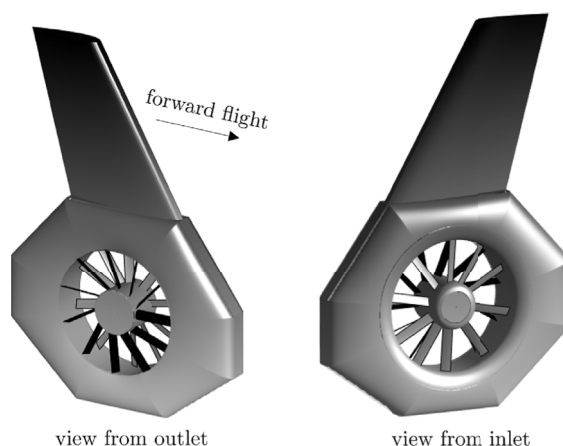
Fig. 1. Typical advanced shrouded tail-rotor concept including the swept fin, viewed from downstream (outlet) and from upstream (inlet). Radial shaft and leant vanes shown on the left view and unevenly-spaced rotor blades shown on the right view.

of irregularly spaced and inclined outlet guide vanes, for both aerodynamic and structural reasons. Complicated aerodynamic interactions take place, leading to the generation of sound further scattered by the under-hood geometry. In another context, the same situation is faced as low-speed and small-size cooling fans separately supplied by manufacturers are installed on electronic racks by means of additional struts. At a very different scale the tower of a wind turbine acts as a free-field source of distortion generating tonal noise in the same way as the transmission shaft for the tail rotor. Though the corresponding frequencies enter the range of infrasound, they could be addressed similarly. Finally modern very-high and ultra-high bypass ratio engines for aircraft propulsion involve heterogeneous outlet guide vanes, mostly because the pylon that supports the engine under the wing is integrated inside the stator. This makes some properties of the generated noise close to those of the tail-rotor. Basic differences about the last two examples are rather on sound propagation. For the wind turbine the main focus is on open long-range propagation through a possibly non-homogeneous atmosphere. For the aircraft engine sound propagation must be primarily considered both inside the inlet and inside the bypass duct prior to outside transmission. This involves a pronounced waveguide effect, unlike the case of the helicopter tail rotor.

The tail rotor is also selected here as a single rotor-stator stage that associates quite complicated mechanisms, rich in terms of underlying physics but quite simple in terms of geometry. Blades and vanes are rectangular and nearly untwisted. Indeed twist would make no sense in view of the wide range of required variable pitch angle of the rotor blades, from zero to maximum flow rate in forward flight and in hover, respectively [1]. The rectangular blade/vane shape has the interest of being very accessible to analytical prediction techniques.

Dealing with sound-generating mechanisms, the present work addresses the tonal noise generated by periodic interactions that result from the relative motion between rotating blades and stationary vanes or struts. The first motivation is that these interactions are intrinsic to the design. Additional aspects due to non-axisymmetric flow ingestion in forward flight or manœuvre, for instance, are not considered as not intrinsic. Broadband noise generated by random interactions of solid surfaces with the turbulence in the flow is not considered either. Focusing on tonal noise is justified by the fact that it is of higher subjective loudness. Furthermore it dominates in configurations where strong flow distortions or interaction mechanisms take place, which is the case in the addressed example. Finally the tonal noise is produced by interfering coherent sources; as such it can be minimized by re-addressing the design. Nevertheless the approach could be transposed to broadband noise investigations at the price of an additional statistical analysis.

With the aforementioned restriction, tonal noise mainly results from two mechanisms associated with the unsteady aerodynamic forces induced on blades and vanes, according to the acoustic analogy [2]. Firstly the stator vanes generate sound because of the periodic impingement of the rotor wakes. This is referred to as wake-interaction noise (WIN) and is the only significant contribution of rotor-stator interaction when the axial distance between the rotor and the stator is large enough, typically more than a quarter chord, which is assumed here. Secondly the rotor blades interact with the potential flow distortion that develops upstream of the transmission shaft, which generates potential-interaction noise (PIN). In homogeneous rotor/stator stages both mechanisms radiate at harmonics of the blade-passing frequency (BPF) defined as the rotational frequency multiplied by the number of rotor blades. As discussed later on, uneven blade spacing applied on the rotor is known to reduce the emergence of the BPF tones for both WIN and PIN, at the price of a regeneration of other multiples of the rotational frequency, which leads to a reduced perceived nuisance. Furthermore with leant stator vanes the impingement of a wake is not simultaneous along the vane span, which reduces the level of WIN by taking benefit from phase cancellations. In all configurations the same tones are emitted by the rotor and the stator by virtue of both addressed mechanisms. This makes the diagnosis of the dominant sources difficult but also raises the question of whether or not part of the noise from one mechanism could be cancelled by the noise from the other one in some configurations. Though this is beyond the scope of the present study, the simple analytical

models presented in the paper are good candidates to answer the question by allowing repeated low-cost and fast-running calculations.

The theoretical basis for tonal-noise analysis is the recognition of its modal structure, according to which the acoustic field of each tone can be expanded as an infinite sum of elementary waves referred to as spinning radiation modes. Each mode has a far-field radiation efficiency determined by a Bessel-function factor, as evidenced by many authors in the past, amongst others [3–5]. Now the uneven blade spacing and the removal of one vane from the stator illustrated in Fig. 1 dramatically redefine interferences between blade/vane signatures, some of which would be destructive in a homogeneous stage. This leads to fundamentally reconsider the modal structures of both PIN and WIN.

The present study is a substantial continuation of previous works [6–8]. It is aimed at demonstrating the ability of simple analytical methods to reproduce the effect of aforementioned three-dimensional design features on the free-field tonal noise. This is the occasion of reviewing a collection of far-field formulas that enable a relevant investigation of all major design effects on tonal noise generation, including sweep, lean, non-compactness and rotor/stator heterogeneity. In fact the only discarded parameters are those defining the precise shape of blade/vane cross-sections, namely thickness and camber. Such parameters are not tractable analytically. Moreover they are often still unspecified at the very preliminary design stage to which the present approach is dedicated. Generic formulae for compact blade/vane segments are first reviewed in section 2 as a theoretical background. The important notion of source-mode is also introduced; it allows synthesizing radiation modes also in the near field. Complete non-compact formulations applicable to advanced design are presented in section 3. The analytical modeling of the source terms in the usual sense of the acoustic analogy is addressed in section 4. Free-field stator noise predictions are detailed in section 5 to illustrate the general approach. The scattering by the shroud is finally considered in section 6. It is predicted for specified source-modes with FEM (Finite-Element Method) simulations and key results are discussed.

2. Basic tonal noise formulations

Elementary expressions to calculate the acoustic pressure radiated by a rotor-stator stage in the far field and in unbounded homogeneous atmosphere are reviewed first in this section. The far-field expressions are used in this work only as a reference for the analysis of the modal properties of the radiated field. In a second step equivalent source modes are introduced, from which the sound field could be expressed uniformly in the whole space. A single source radius is considered first for simplicity but a complete formulation will be used later on.

2.1. Model tail rotor

For the assessment of technological effects, some of the analytical models proposed in this work are implemented on a representative test-case of tail rotor with various versions, inspired by the sketch in Fig. 1. The blade number is $B = 10$ and the vane number is either $V = 11$ or $V = 10$ depending on whether the shaft is considered in place of a vane or not; in any case the angular vane spacing is therefore $2\pi/11$. In the baseline configuration (Fig. 2-a) the rotor is homogeneous, whereas it has uneven blade spacing in an advanced version according to the distribution shown in Fig. 1, each blade of number j being displaced by $\alpha_j = \nu \sin(4\pi j/B)$ from its regular blade angle $j2\pi/B$ in the rotor frame, ν being a constant. This ensures the geometrical symmetry with respect to a diameter. As a result all even multiples of the rotational frequency will be expected in the sound field instead of the BPF harmonics. Furthermore the stator vanes can be either radial or with a lean angle of $\zeta = 30°$. The blades and vanes are assumed rectangular flat plates. Their equivalent stagger angles are defined with respect to the rotation plane. The rotor stagger angle γ can vary and the vane angle is set to $\gamma' = 70°$. The hub radius is $r_H = 12.5$ cm and the tip radius is $r_T = 42$ cm, corresponding to a radial extent of 29.5 cm and a leant-vane span L of 30 cm. The chord length c, identical for the blades and the vanes, is of 6 cm, which corresponds to an aspect ratio $L/c = 5$.

The stationary reference frame shown in Fig. 2-a has the center of the circular path of any mid-chord point as origin. According to the strip-theory approach, the unsteady aerodynamics of blades and vanes is described in unwrapped cylindrical cuts as illustrated in Fig. 2-b. This allows using two-dimensional models the parameters of which are functions of the radius r. The cascade representation in Fig. 2-b introduces the main notations involved in the definition of the rotor-stator stage, in particular the velocity triangle at rotor exit and its deformation due to the velocity deficit in the wake.

The rotation is in the counterclockwise direction and the $\mathbf{e}_Z$ axis is oriented towards the inlet side. Two rotational speeds Ω are considered, 2920 rpm and 4500 rpm, in order to also shortly address the effect of rotational frequency at equal modal structure. The BPF of the rotor in its homogeneous version is 487 Hz or 750 Hz depending on Ω and the blade-tip tangential speed is 128 m/s or 198 m/s (tip Mach number $M_t = 0.38$ or 0.58). The analysis is limited to the first three BPF harmonics, thus below 2.25 kHz, so that the chord-based Doppler-corrected Helmholtz number ranges up to

$$\frac{cmB\Omega}{c_0(1 - M_t)} = \frac{k_{mB}c}{1 - M_t} \simeq 6$$

where $k_{mB} = mB\Omega/c_0$ is the acoustic wavenumber and c_0 the sound speed, for the harmonic order $m = 3$. This means that chordwise non-compactness must be accounted for in the models at high frequencies.
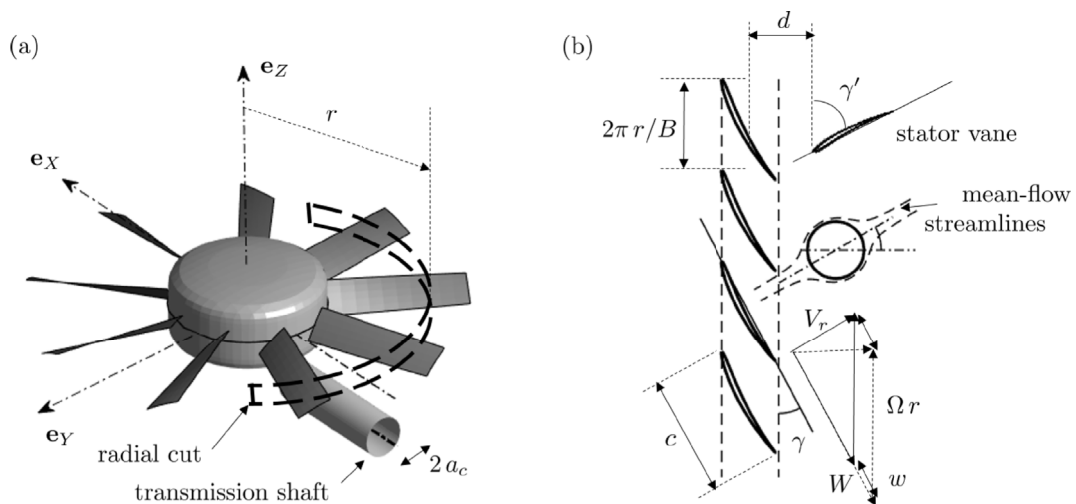
Fig. 2. (a): three-dimensional view of a homogeneous tail rotor (shroud and stator vanes not shown) with main axes; (b): unwrapped cut of a strip of mean radius r showing the main parameters and featuring the velocity triangle and its deformation in a blade wake. W is the mean-flow speed relative to a blade and w the velocity deficit in a wake.
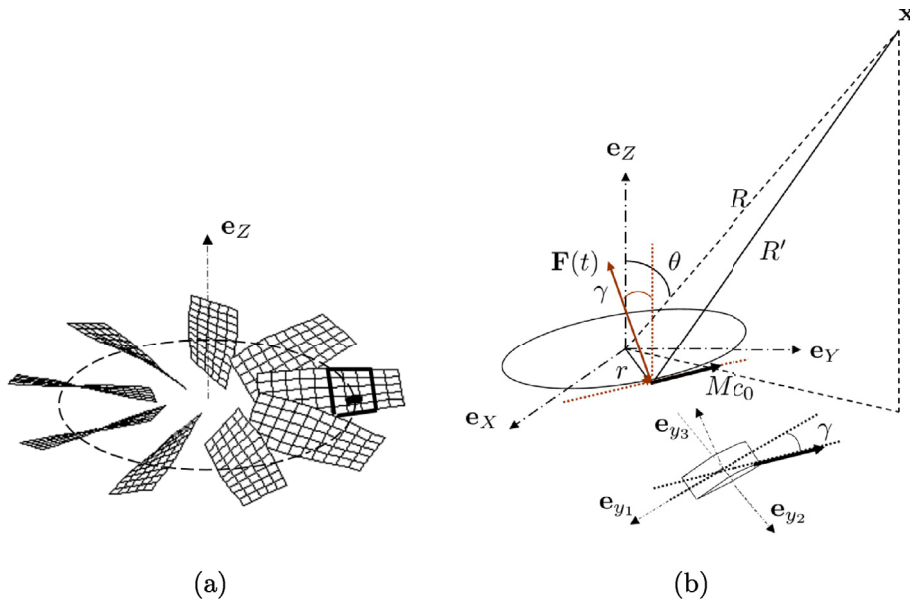

Fig. 3. (a): schematics of the mean-camber surface of a rotor made of thin blades, featuring a blade element as the black patch and a blade segment as the thick trapezoid. (b): reference frame for rotor-noise problem statement, featuring the global coordinates with origin at the center of the circular path of a blade element and the local coordinates (y_1, y_2, y_3) in a reference frame attached to a blade segment centered on this element.

2.2. Generic formulae

The free-field tonal noise of a rotor in the presence of a stationary azimuthal distortion is generated by blade forces that are periodic with the period of rotation [9] when described in a reference frame attached to a blade. This is the case here with the potential field of the transmission shaft. Viscous forces are neglected in aeroacoustic problems and the blade forces reduce to pressure forces distributed over the surface of the blades. In most simplified problem statements involving thin blades, such as for fans and compressor stages, the forces are further reduced to the lift distributed over the mean-camber surface assuming zero thickness. For practical implementation, this surface must be discretized in acoustically compact elements (black cell in Fig. 3-a) and an unsteady lift force must be specified on each element. Generic expressions can be derived for the sound radiated by the element and the total sound field is then obtained by linear superposition.

Let us consider first a homogeneous rotor with B blades, thus only emitting the harmonics of the BPF, and the periodic array of dipoles rotating on a circle of radius r made of the same blade element repeated on each blade and considered as a point source.

Assuming a reference frame with origin at the center of the circle (similar to the sketch in Fig. 3-b), the complex amplitude of the acoustic pressure produced by the array in the far field at the BPF harmonic of order m can be expanded as the sum of radiation modes [7]

$$p_{mB}(\mathbf{x}) = \frac{i\,k_{mB}B}{4\pi R}\,e^{i\,k_{mB}R}\sum_{s=-\infty}^{\infty} F_s\,e^{i(mB-s)(\varphi-\pi/2)}\,J_{mB-s}\left(k_{mB}r\sin\theta\right)\left[\cos\theta\,\cos\gamma - \frac{(mB-s)\,\sin\gamma}{k_{mB}r}\right] \tag{1}$$

where spherical coordinates (R, θ, φ) are used for the observer. The factors F_s are the Fourier coefficients of the point lift force or dipole strength on the element, defined by the discrete Fourier transform

$$F(t) = \sum_{s=-\infty}^{\infty} F_s\,e^{-i\,s\Omega\,t}, \qquad F_s = \frac{\Omega}{2\pi}\int_0^{2\pi/\Omega} F(t)\,e^{i\,s\Omega\,t}\,dt\,.$$

The formula assumes that the point dipole on a blade chosen as reference is exactly on the $\mathbf{e}_X$ axis at the origin of time. The total sound produced by the rotor can be obtained from Eq. (1) by further performing a double sum on all elements of a discretized blade, applying an axial and tangential phase correction to the contribution of each element to account for its different position at the origin of time. This equivalently accounts for the propagation-path differences, as described for instance by Hanson and Parzych [10]. The double sum does not question the interference properties already expressed by Eq. (1).

This fully discretized approach is unavoidable when the mean-camber surface is actually described as a realistic curved surface and when the description of the complex-valued periodic lift is deduced from the post-processing of numerical flow simulations, for instance. It is also well suited when modeling diffraction effects that are a matter of relative distance between source points and scattering surfaces, as will be seen in section 6.

In absence of accurate description of camber and/or lift distribution, which is the framework of the present work and of preliminary design studies, a blade can be split into segments defined by cylindrical cuts of neighboring radii. Such a segment is featured as the thick-line trapezoid in Fig. 3-a. Assimilating the segment to a rectangular flat plate of small aspect ratio, the chordwise integration can be performed analytically, leading to closed-form expressions for both the distributed lift on the segment and its contribution to the far-field sound. This fully analytical approach turns out to be a useful alternative, provided that an explicit model for the distributed lift is available. Relevant models will be the matter of section 4. Typically for a segment of elementary span and mean radius r the unsteady lift is written as a function of the chordwise coordinate y_1 from leading edge to trailing edge, say $\widetilde{\ell}_s(y_1)$, in the rotating reference frame in Fig. 3-b. It is first weighted by a phase term that accounts for the chordwise differences of propagation path to the observer and next integrated from leading edge to trailing edge. Eq. (1) still holds, replacing the factors F_s by the quantities still noted $F_s(r)$ and expressed as

$$F_s(r) = \int_{-c/2}^{c/2} \widetilde{\ell}_s(y_1)\,e^{i\,A_s y_1}\,dy_1 \tag{2}$$

with

$$A_s = k_{mB}\cos\theta\,\sin\gamma + (mB-s)\frac{\cos\gamma}{r}\,.$$

These quantities are referred to as the blade-loading harmonics (BLH) in this work, though they combine both the actual aerodynamic loading and the sound-propagation effect, accounting for chordwise non-compactness [9]. The formulation also implies that the circular cut of a blade at radius r is assimilated to a straight segment, which makes sense for moderate numbers of blades at two conditions. Firstly the blade cross-section must be of small camber and thickness. Secondly the chord must be much shorter than the perimeter of the circle of radius r.

The time dependence is $e^{-imB\Omega t}$, so that the phase of a single radiation mode in the sum in Eq. (1) is

$$e^{-i\,mB\Omega\,(t-\varphi/\Omega_s)} \qquad \text{with} \qquad \Omega_s = \frac{mB\Omega}{mB-s}\,.$$

This defines a spinning pattern of angular phase speed Ω_s with $n = mB - s$ lobes. Eq. (1) with the chordwise integrated BLH $F_s(r)$ holds in a reference frame with origin at the center of the circular path of the mid-chord point of the considered blade segment (see Fig. 3-b). It must be noted that in general the BLH and the stagger angle γ depend on the radius, even though for the tail rotor the twist is negligible and this angle will be assumed constant. The complete sound field is obtained from Eq. (1) by further performing integration along the span, from the hub radius r_H to the tip radius r_T. The formal simplicity highlights the radiation efficiency of the modes, determined by the Bessel functions. It illustrates the standpoint of a far-field observer in the sense that the distance is large when compared to both the wavelengths and the tip radius of the blades. Expressions of the sound field that are uniformly valid in whole space can also be derived [11]. They are not reproduced here for conciseness but of course correspond to the same modal structure in terms of number of lobes and spinning phase speeds.

The formulation of the tonal noise of a homogeneous stator of V vanes at the same BPF harmonic caused by the periodic impingement of the rotor wakes at the radius r is achieved following similar principles. It takes the simpler form of a finite sum over the number of vanes, starting from the formula for a stationary dipole. A vane is discretized in compact elements and the same element taken on each vane if a fully discretized approach is needed. Otherwise the vanes are just split into flat-plate segments for analytical modeling. For convenience the origin of the reference frame is displaced at the center of the mid-chord
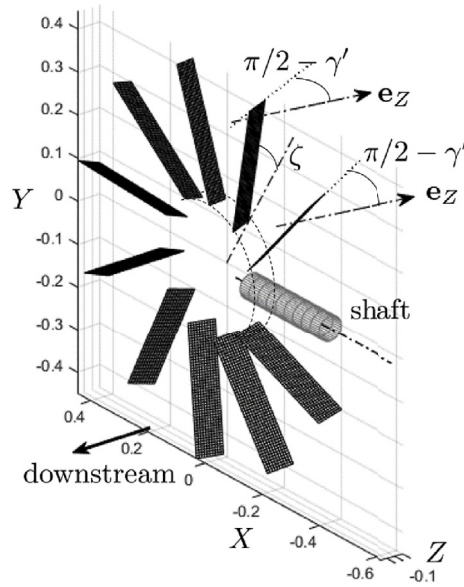
Fig. 4. Sketch of the stator configuration of the advanced tail rotor, showing the lean angle ζ and the stagger angle γ'. Transmission shaft plotted in gray (ignored in the calculations), to be replaced by an additional vane for the complete stator configuration.

circles of the array of segments, keeping the same notations for the observer coordinates. This allows a clear comparison of the radiating properties of the rotor and of the stator. The far-field sound pressure reads

$$p_{mB}(\mathbf{x}) = \frac{\mathrm{i}\, k_{mB}}{4\pi R}\, \mathrm{e}^{\mathrm{i}\, k_{mB}R}\, F_{mB}(r) \sum_{j=0}^{V-1} \left[\cos\gamma'\,\cos\theta - \sin\gamma'\,\sin\theta\,\sin\left(j\frac{2\pi}{V}-\varphi\right)\right]$$

$$\times \exp\left\{\mathrm{i}\, mB\left[j\frac{2\pi}{V} - \sin\theta\,\frac{\Omega r}{c_0}\,\cos\left(j\frac{2\pi}{V}-\varphi\right)\right]\right\} \tag{3}$$

where the stagger angle γ' corresponding to the dipole force inclination is still counted positive (as for γ) though the orientation is opposite (see Figs. 2 and 4). Mathematically this expression is equivalent to

$$p_{mB}(\mathbf{x}) = \frac{\mathrm{i}\, k_{mB}V}{4\pi R}\, \mathrm{e}^{\mathrm{i}\, k_{mB}R}\, F_{mB}(r) \sum_{s=-\infty}^{\infty} \mathrm{e}^{\mathrm{i}\,(mB-sV)(\varphi-\pi/2)} J_{mB-sV}\left(k_{mB}r\sin\theta\right) \left[\cos\theta\,\cos\gamma' + \frac{(mB-sV)\sin\gamma'}{k_{mB}r}\right], \tag{4}$$

which emphasizes the similarity with Eq. (1). This means that both mechanisms have the same modal structure. In fact the spinning modes of free-field radiation can be thought of as a complete set of fundamental wave forms that can be used to describe the tonal sound field from rotating-blade technology.

2.3. Source-modes

The acoustic field of an isolated spinning radiation mode from Eqs. (1) and (4) can be alternatively obtained from a continuous distribution of stationary, phase-shifted dipoles on the circle of radius r. Furthermore this exact mathematical identity does not reproduce only the far field. It generates a uniformly valid description in the entire space, as shown in Ref. [11]. The distributed dipoles must have the same inclination γ or γ' as the lift forces. For instance, at the point-source location α on the circle, the dipole strength equivalent to the force $\mathbf{F}(t)$ in Fig. 3-b is

$$F(\alpha, t) = F\left(0, t - \frac{(mB-s)\,\alpha}{mB\Omega}\right)$$

with $F(0, t) = F_s \mathrm{e}^{-\mathrm{i}mB\Omega t}$, F_s being the Fourier harmonic of order s.

For practical implementation this circle distribution, called source-mode in the present work, is discretized; the radiated field is simply synthesized by linear superposition. This means that the azimuthally discretized source-mode can be understood as a virtual stator with an arbitrary large number of vanes even in the case of rotating sources. In the reference frame in Fig. 3, the free field of a point dipole extracted from a circular source-mode at the angle α is expressed by the scalar product of the

(a) BPF mode $n = -1$ (b) BPF mode $n = 10$

(c) 2BPF mode $n = -2$ (d) 2BPF mode $n = 9$
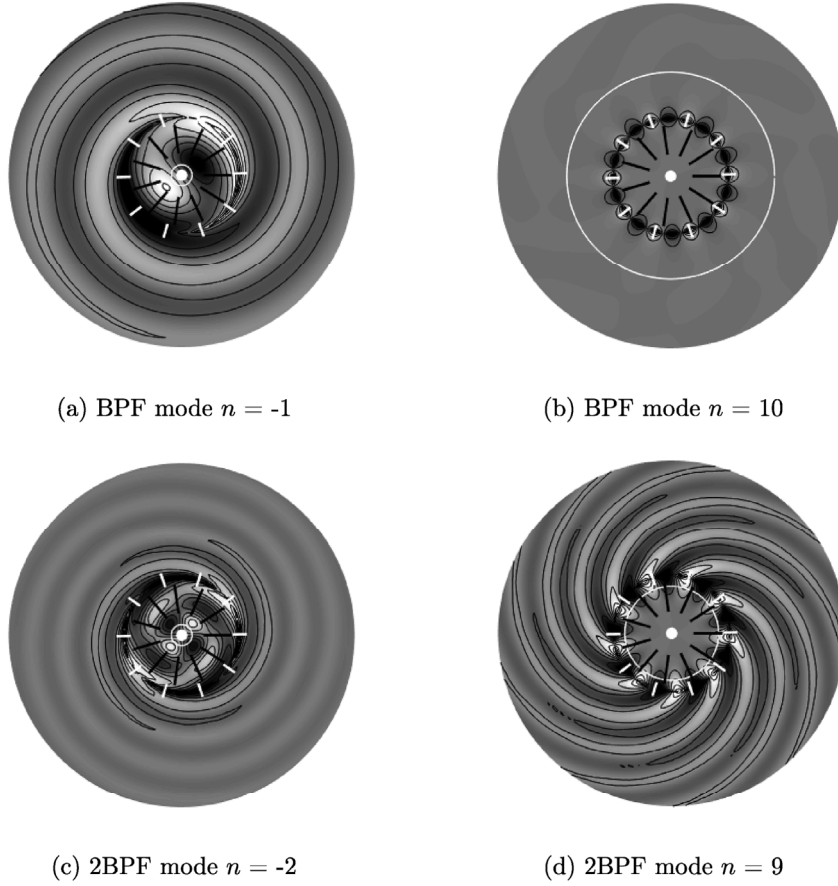
Fig. 5. Instantaneous pressure patterns of isolated radiation modes generated by the baseline tail-rotor model in the mid-chord plane of the stator of coordinates (X, Y), at the first two BPF. Light and dark areas stand for over- and under-pressures. Blade ($B = 10$) and vane ($V = 11$) locations featured by white and black radial segments, respectively. Sonic circle plotted in white. Same arbitrary amplitude scale for all plots.

dipole strength by the gradient of the free-space Green's function for the Helmholtz equation G, as [11].

$$\mathbf{F}_s \cdot \nabla G = \frac{F_s(\alpha)R}{4\pi R_\alpha^3} e^{i\,k_{mB}\,R_\alpha} (1 - i\,k_{mB}\,R_\alpha) \left[\sin\gamma\,\sin\theta\,\sin\gamma\,\sin(\varphi - \alpha) - \cos\gamma\,\cos\theta\right],$$

R_α standing for the observer's distance to the stationary point source at angle α. The uniformly-valid expression of $\mathbf{F}_s \cdot \nabla G$ is used to compute the results in the rotation plane $\theta = \pi/2$ shown in Fig. 5 and those on an observation sphere shown later in Fig. 13.

The aforementioned formal identity has two advantages. Firstly the source-modes provide a clear understanding of the wavefront structure and of the radiating properties of a single mode, as discussed below. Secondly, because diffraction prediction tools are usually formulated in the frequency domain for stationary sources, they can be applied separately to all stationary constituting sources of a discretized source-mode to compute its diffraction by an obstacle of arbitrary shape [11]. Installation effects can then be investigated. This will be applied in section 6.

The behavior of isolated modes in the stator mid-chord plane $\theta = \pi/2$ is illustrated in Fig. 5 for the rotor-stator interaction mechanism, in the baseline configuration with $B = 10$ and a complete stator with $V = 11$ vanes, for a source radius of 40 cm and only one identical compact element on each vane. The coordinates are those in the reference frame of the stator. Tyler & Sofrin's rule selects the modes $n = mB - sV$ at the mth BPF harmonic, s being any relative integer. Only the smallest values of $|n|$ are retained as the orders of dominant modes, typically $n = -1$ and $n = 10$ at the BPF and $n = -2$ and $n = 9$ at twice the BPF. A particular property is that the tangential phase speed at the source radius must be supersonic for the radiation to be efficient. In Fig. 5 this supercritical (supersonically spinning) or sub-critical (subsonically spinning) character of the modes is clearly identified. The supersonic condition also writes $\Omega_s r/c_0 > 1$ or

$$mBM > mB - s \quad \text{with} \quad M = \Omega r/c_0,$$

which means that the argument of the Bessel function is larger than its order. It is also convenient to introduce the sonic circle, the radius of which corresponds to a tangential phase speed equal to the speed of sound for the same mode. A supercritical
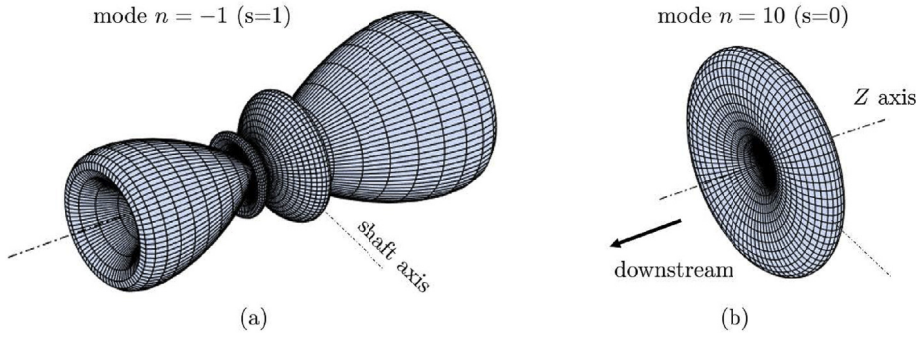
Fig. 6. Directivity patterns of the first two modes at the BPF (see Fig. 5-(a) and (b)), rear view. Rotor axis Z and shaft axis shown as dashed-dotted lines. (a): efficient mode; (b): rotor-locked 'cut-off' mode (much lower amplitude).

mode produces spiral wavefronts in its rotation plane, as recognized in Fig. 5-(a),(c) and (d), where it is also checked that the sonic circle plotted in white is smaller that the source circle. In the opposite case the subsonic phase speed only forces a nearly evasnescent wave because the Bessel function is approaching zero. This is what is observed in Fig. 5-(b) for the mode $n = 10$ at the BPF ($s = 0$): pressure fluctuations concentrate close to the source circle but rapidly vanish away from it, even inside. The sonic circle is well beyond the source circle. It is also worth noting that the mode $n = 10$ ($s = 0$) can be said rotor-locked because its spinning phase speed is equal to the rotational speed Ω.

As a complementary illustration, the three-dimensional directivity patterns of the two modes in Fig. 5-(a) and (b), determined from sound calculations on an observation sphere, are plotted in Fig. 6, again in the reference frame of the stator. The observer's position is close to that in Fig. 1-a. The mode $n = 10$ radiates poorly with a single lobe normal to the axis in the meridian plane, which features a toroidal pattern. Because in a duct this source property would only excite cut-off modes, the mode $n = 10$ can also be said cut-off by extension. In contrast the efficient mode $n = -1$ radiates dominantly at an acute angle from the axis, which would correspond to a cut-on mode inside a duct. In a tail-rotor configuration this mode is *a priori* less affected by the shroud but it should not be a matter of concern for an observer under the flight path of a helicopter because it poorly radiates normal to the axis. The complete sound field at any multiple of the BPF is made of a combination of such modes, the relative phases and amplitudes of which determine additional three-dimensional features. This will be discussed in more details in section 5 for stator noise.

3. Complete rotor-noise and stator-noise models

This section addresses extensions of previous formulae that take the full span and the possible heterogeneity into account. A spanwise integration is added according to the strip-theory approach, in which parameters such as, for instance, the angular position of a vane element can be defined as functions of the radius r. Uneven blade spacing on the rotor must also be formulated.

3.1. Far-field rotor-noise formula

General formulae are derived first to predict the rotor tonal noise caused by the potential distortion around the transmission shaft. The description of the distortion (section 4.1) and the introduction of uneven blade spacing are key steps. The model is not applied in the paper for conciseness but all steps of the method are described referring to previous works by the authors; they can be implemented simply. Uneven spacing has also been addressed by other investigators, for instance Refs. [13–15]. In the case of a rotor with uneven blade spacing, the same expression as Eq. (1) holds for any strip of radius r replacing the BPF harmonic by any multiple of the rotational frequency, except that the first factor B must be replaced by an interference sum, noted I_N below [12]. Accounting for the integration over the full span, the general expression becomes

$$p_N(\mathbf{x}) = \frac{ik_N}{4\pi R} e^{i k_N R} I_N \int_{r_H}^{r_T} \sum_{s=\infty}^{\infty} F_s(r) e^{i(N-s)(\varphi-\pi/2)} J_{N-s}(k_N r \sin\theta) \left[\cos\theta \cos\gamma - \frac{(N-s)\sin\gamma}{k_N r}\right] dr, \quad (5)$$

with

$$I_N = \sum_{j=0}^{B-1} e^{-i N(\alpha_j + j\,2\pi/B)}.$$

It must be kept in mind that in the case of a homogeneous rotor, when all coefficients α_j are zero, this sum is just B if N is a multiple of B and zero otherwise. It ranges between these extreme values for a rotor with uneven blade spacing. The modal structure of the interaction is modified; it is now expressed by the phase and spinning speed of each term in the s-sum

$$e^{-i N\Omega(t-\varphi/\Omega_s)} \quad \text{with} \quad \Omega_s = \frac{N\Omega}{N-s}.$$
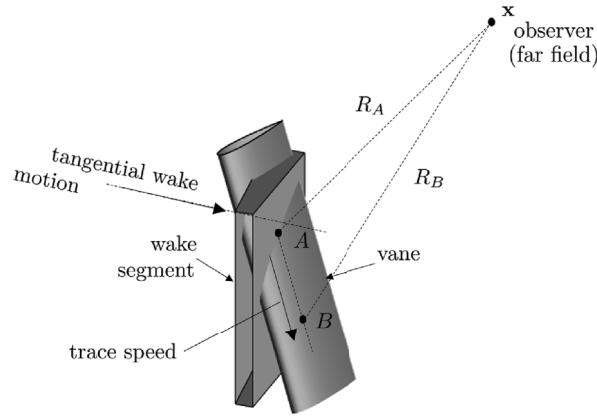
Fig. 7. Wake impingement on a leant stator vane.

An important general property is that the modal structure in terms of number of lobes and rotational phase speeds does not depend on whether the radial and/or chordwise integration is performed or not. It is only a matter of summed similar terms with different phases, so that the key modal features of the sound field are already obtained with only one source radius or with only the same point source taken on each blade instead of the complete blade surface. This property holds as well for arrays of stationary vanes; it will be used in section 6 for simplified stator noise assessment. In fact interferences can be managed at two levels for noise control. The first level is that of the number and positions of blades, the rotor acting as a circular array of coherent point sources. The second level is the surface integration that introduces other possible cancellations because of chordwise and spanwise phase differences in the received elementary sounds.

3.2. Far-field stator noise formula

General formulae for stator noise are detailed now, with application to the advanced design depicted in Fig. 1. The concept of leant or swept stator vanes for the reduction of tonal wake-impingement noise has been addressed in many studies dealing with low-speed fans or with modern, high-speed turbofan architectures, amongst others [16,17]. The mechanism is twofold and essentially depends on aerodynamic and acoustic compactness notions illustrated in Fig. 7 for a radial (vertical) wake and a leant (oblique) vane. As the wake segment moves along its tangential path in this representation, its interaction with the vane is characterized by a finite spanwise trace speed. If two associated source points A and B are considered with respect to a far-field observer at some point $\mathbf{x}$, this trace speed, say U_t induces a phase lag expressed by the factor $e^{i\omega\,\delta_s/U_t}$ at the angular frequency ω if δ_s stands for the distance between A and B. The different propagation distances R_A and R_B to the observer introduce another phase-lag factor $e^{ik(R_A-R_B)}$ with $k = \omega/c_0$. Both lags can be positive or negative. Possible cancellation between sounds received from A and B occurs if the cumulated phase lag $k(R_A - R_B) + \omega\,\delta_s/U_t$ is of the same order of magnitude as π or larger. No significant cancellation is expected if it is much smaller than π. Parallel wakes and vanes would correspond to simultaneous impingement along the span ($U_t = \infty$), which is a recognized detrimental condition. The portion of vane of length δ_s is said acoustically compact if $k\delta_s \ll \pi$, in which case it can be replaced by an equivalent point dipole. But the strength of this dipole can be reduced by the lean angle for a given wake pattern because of opposite or substantially shifted phases of the unsteady lift at points A and B. The portion of vane is said aerodynamically compact only if $\omega\,\delta_s/U_t \ll \pi$. These properties are fundamental for the control of the tonal noise. They can be transposed to rotor swept blades, not considered in this work.

For small-size and low-speed cooling fans of electronic racks at the first BPF harmonics, the vanes are acoustically compact, in the sense that spanwise sound-path differences are small enough when compared to the wavelengths to have a weak effect on the far-field sound. The main benefit of lean/sweep results from aerodynamic non-compactness. At higher speeds and frequencies or for larger vanes, the sound-path differences also induce significant phase shifts between received sounds from various vane segments, which leads to another possible reduction by destructive interferences. Both effects on the source distribution and on the sound-path differences compete, so that the cancellations are not simply cumulative. For this reason they must be both modeled in a unified approach. To summarize, vane lean is a relevant reduction mean for the tail-rotor for two reasons. Firstly, the blades are radial with nearly no twist, therefore all sources of wake-interaction noise would be in-phase all along the span with radial vanes. Secondly, the vanes are not acoustically compact.

As stated in section 2.2 the acoustic pressure generated by stator-noise sources located at a given radius can be expressed in two equivalent ways, either as a sum of spinning radiation modes or as the summed fields of V stationary dipoles. The second view is better suited for scattering studies. In that sense the stator can also be interpreted as an under-sampled source-mode discretization. However the first view clearly highlights the modal structure. Finally both formulations are retained to analyze stator noise.

The sound pressure radiated in the far field by the incomplete stator of leant and regularly spaced vanes at the harmonic of order m of the BPF for a homogeneous rotor is therefore expressed by its complex amplitude

$$p_{mB}(\mathbf{x}) = \frac{\mathrm{i}\,k_{mB}}{4\,\pi\,R}\,\mathrm{e}^{\mathrm{i}\,k_{mB}\,R} \int_{r_H}^{r_T} F_{mB}(r) \sum_{j=1}^{V-1} \left[\cos\gamma'\,\cos\theta - \sin\gamma'\,\sin\theta\,\sin\Theta_j\right]\,\mathrm{e}^{\mathrm{i}\,mB\,[\Theta_j + \varphi - \sin\theta\,\Omega\,r\,\cos\Theta_j/c_0]}\,\mathrm{d}r \tag{6}$$

with

$$\Theta_j = j\frac{2\,\pi}{V} + \psi(r) - \varphi\,,$$

$F_{mB}(r)$ being the chordwise-integrated vane loading harmonic and $k_{mB} = mB\Omega/c_0$. $\psi(r)$ denotes the angular deviation of a point of a leant vane from its location in a zero-lean case. The same expression is valid for any multiple of the rotational frequency in the case of a heterogeneous rotor, just replacing mB by any integer N. In the present case $\psi(r)$ is such that

$$\frac{\sin\psi(r)}{\sin\zeta} = \frac{\ell'(r)}{\left[\ell'^2(r) + r_H^2 + 2r_H\,\ell'(r)\,\cos\zeta\right]^{1/2}}$$

if ζ denotes the lean angle of the vanes, positive by convention, and $\ell'(r)$ the distance from the hub to the current source point along the vane span

$$\ell'(r) = \left[r^2 - r_H^2\,\sin^2\zeta\right]^{1/2} - r_H\,\cos\zeta\,.$$

The negative value of $\psi(r)$ corresponds to vanes that are leant in the direction opposite to the rotation of the blades. The far-field expression of the stator noise can be equivalently rewritten in the form of an infinite sum of spinning radiation modes, which, further introducing the radial integration, yields

$$p_{mB}(\mathbf{x}) = \frac{\mathrm{i}\,k_{mB}}{4\,\pi\,R}\,\mathrm{e}^{\mathrm{i}\,k_{mB}\,R} \int_{r_H}^{r_T} F_{mB}(r) \sum_{n=-\infty}^{\infty} \mathrm{e}^{\mathrm{i}n\,(\varphi - \pi/2)}$$

$$\times \mathrm{J}_n\left(k_{mB}r\,\sin\theta\right) \left[\cos\gamma'\,\cos\theta + \frac{n\,\sin\gamma'}{k_{mB}\,r}\right]\,\mathrm{e}^{\mathrm{i}(mB-n)\,\psi(r)} \sum_{j=1}^{V-1} \mathrm{e}^{\mathrm{i}(mB-n)\,j\,2\pi/V}\,\mathrm{d}r \tag{7}$$

The interference sum over the index j is incomplete. If started from $j = 0$ it would be exactly V when $mB - n$ is a multiple of V and 0 otherwise, then recovering the classical Tyler & Sofrin's rule. Here the sum is either $V - 1$ or -1, respectively, so that all possible spinning modes are generated. The ten-times lower value of the sum when $mB - n$ is not a multiple of V can be balanced only by a stronger weighting by the Bessel function. This is why the efficiency factor defined as

$$\mathrm{J}_n\left(k_{mB}r\,\sin\theta\right) \sum_{j=1}^{V-1} \mathrm{e}^{\mathrm{i}(mB-n)\,j\,2\pi/V}$$

is plotted as a key quantity in Fig. 8 for some parameters and an indicative observation angle of 45°. At the BPF of the homogeneous rotor $(m = 1)$, $N = B$ and the highest value is obtained for $n = -1$ thus $B - n = 11 = V$, at the lower speed. At twice the BPF the value $V - 1$ of the interference sum would be obtained for $n = 9$ but it cannot lead to a significant value of the efficiency factor because the Bessel function is close to zero for that order. For the modulated rotor, all even harmonics of the rotational frequency are produced. The efficiency factor can reach quite large values, here typically for $N = 12$ $(n = N - V = 1)$ or $N = 16$ $(n = N - V = 5$ and $n = N - 2V = -6)$, which is specific of the acoustic signature of uneven blade spacing. It is also clear that the actual efficiency is a matter of rotational speed and angle of observation, both involved in the argument of the Bessel function.

4. Source models

Analytical modeling of rotor and/or stator noise based on the acoustic analogy relies on a two-step approach. As a first step the velocity disturbances relative to a blade or to a vane, needed as input, are specified from closed-form expressions available for generic flows. The fluctuating lift forces induced on the blades or vanes by the variations of the relative velocity are derived using linearized unsteady aerodynamic theories. These forces are equivalent acoustic dipoles. Their sound radiation is calculated in a second step according to classical linear acoustics. The aeroacoustic problem is solved as the chaining of aerodynamic and acoustic transfer functions in the frequency domain. This section separately reviews typical models for the velocity disturbances and for the corresponding dipole strengths.
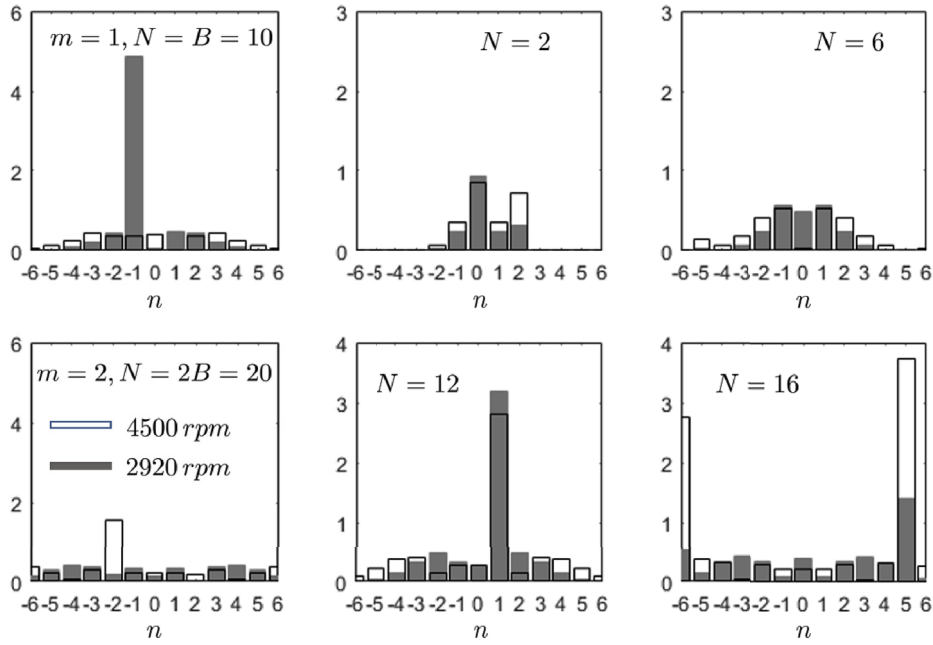
Fig. 8. Bar graphs of the efficiency factor of the incomplete stator, for the first two BPF harmonics of the homogeneous rotor (left plots) and some tones $\omega = N\Omega$ of the modulated rotor. Slow (gray bars) and fast (empty bars) rotational speeds considered. $\theta = 45°$. Negligible values outside the harmonic range $[-6; +6]$.

4.1. Model potential distortion

For a relevant assessment of the rotor noise due to the vicinity of the transmission shaft, the potential velocity distortion upstream of the shaft must be characterized, as required input data in the model. The same need is faced in various similar situations, typically for the low-speed car-engine cooling fan operating with bluff struts closely downstream of the blades or for the wind-turbine because of the tower. In absence of accurate simulations useful estimates are provided by assimilating the real flow at a given radius to the two-dimensional potential flow around a circle, the relative mean-flow velocity V_r and its direction being determined by the velocity triangle at rotor exit (see Fig. 2). The interest is that the time-Fourier coefficients of the periodic upwash experienced by a blade at the trailing edge, called distortion harmonics and noted w_s, can be derived analytically from this flow model. Parametric studies can then be performed readily to investigate the effect of the interaction distance or of the stagger angle of the blades γ. Even in this simple framework the derivations, based on extensive use of the residue theorem, are cumbersome; they are detailed in Ref. [7]. A consistent approximation is used instead in the present work, interpolating a set of exact results for 6 configurations of increasing stagger angle $(10°,14°,20°,25°,29°,35°)$. For illustration the upwash $w(t)$ experienced by the trailing-edge part of a rotor blade for one passage in the extreme configurations $1 (\gamma = 10°)$ and $6 (\gamma = 35°)$ at 2920 rpm, extracted from the potential velocity field of the distortion, is shown in Fig. 9. It is short enough compared to the rotational period to be repeated and periodized by an infinite sum to calculate the distortion harmonics w_s by discrete Fourier transform. As expected, a much stronger impulse will be produced on the blades for the larger angle 35° representative of static flight (hover) conditions, for which the maximum thrust is required. Indeed the trailing edge gets quite close to the shaft. In contrast a weak impulse is produced for the lower angle 10° rather corresponding to forward flight conditions and for which the blade trailing edges are farther away from the shaft; a minimum thrust is required in this case because the anti-torque force is achieved with the fin. The exact real and imaginary parts of the coefficients w_s are plotted in Fig. 10-a, where different symbols are used for the even and odd orders, respectively, to illustrate the alternate positive and negative values. The harmonic spectrum is reasonably interpolated by an expression of the form

$$w_s = (a_R - i\,a_I)(-1)^s\,s\,e^{-s/b}. \tag{8}$$

Once repeated for the 6 configurations the interpolation provides the values of the parameters reported in Fig. 10-b. $|a| = (a_R^2 + a_I^2)^{1/2}$ is found nearly constant; b appears as close to the order of maximum amplitude and is an increasing function of the stagger angle. Indeed as the latter increases the aerodynamic excitation gets stronger.

Though it has been derived for a circular cylinder and for the present parameters, Eq. (8) would probably hold as well for any bluff body located just downstream of a fan rotor, provided that the coefficients are adjusted. Indeed the general features of the potential field upstream of an obstacle, illustrated by the trends in Fig. 10-b, may be similar for very different cross-section shapes. Once tuned on a test case, for instance by comparing with a reference numerical simulation of the flow, the model could be used for repeated low-cost acoustic predictions.
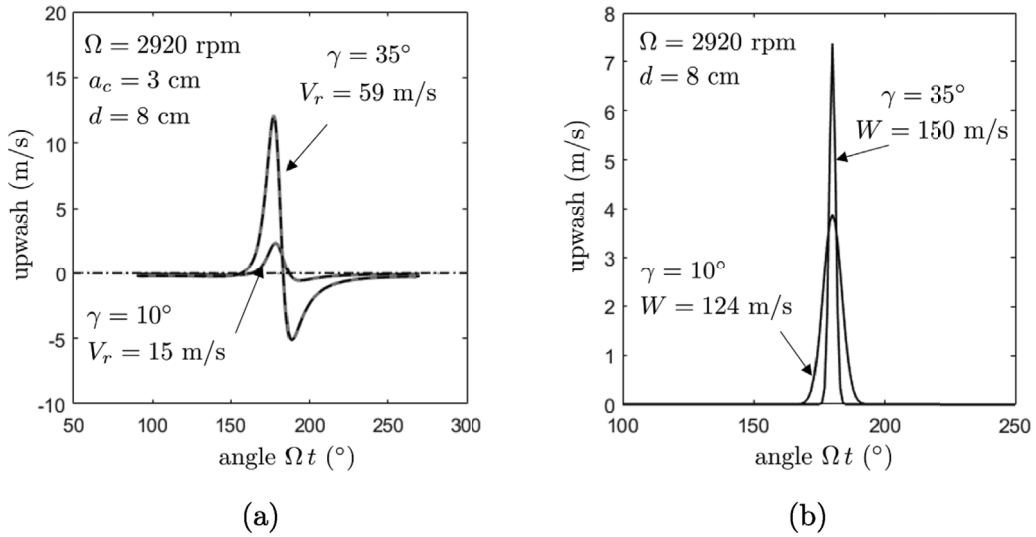
Fig. 9. (a): upwash (velocity fluctuation projected normal to the blade) at the rotor trailing edge due to the potential distortion around the transmission shaft in configs. 1 and 6. Original (dashed-black) and reconstructed (gray) by inverse Fourier transform. (b): model wake velocity-deficit upwash experienced by the leading edges of the stator vanes in configs. 1 and 6, according to Reynolds' et al. model [18]. Parameters indicated on the plots.
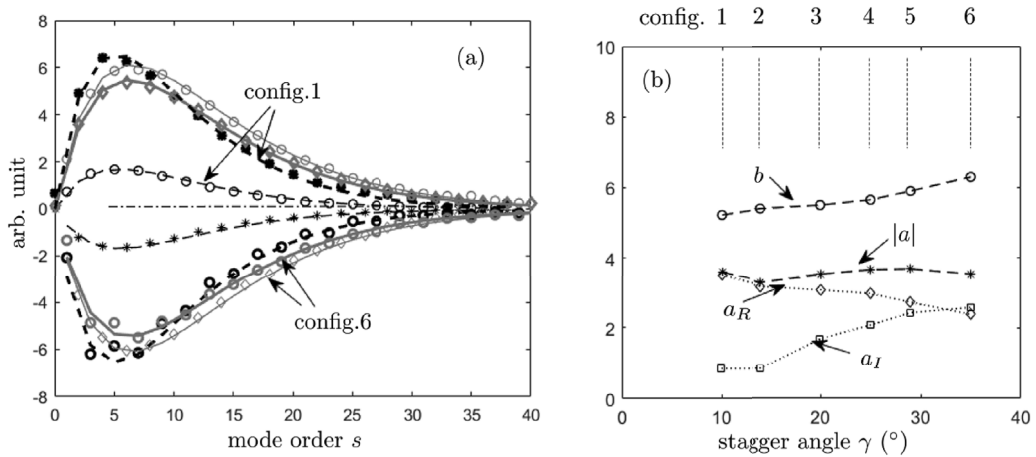

Fig. 10. (a): distortion-harmonic spectra caused by the transmission shaft in config.1 (gray) and config.6 (black) and interpolation using Eq. (8). a_R in thick lines, bold symbols (◇ and ○ for even and odd orders in config.6; * and ○ for even and odd orders in config.1); a_I in thin lines and symbols. (b): Variations of the parameters of Eq. (8) with the stagger angle γ.

4.2. Wake model

The velocity deficit in the wakes of the rotor blades, in the direction of the relative velocity W (Fig. 2), is now the required input for the calculation of stator noise. Again in absence of any accurate information it can be reasonably assumed as Gaussian for mathematical tractability, so that the upwash experienced by a vane due to the passage of a single wake has the form

$$w(t) = w_d\, e^{-\xi\,(t/\tau)^2}$$

where τ is a characteristic wake-passing time, w_d the deficit on the wake centerline and $\xi = \ln 2$. In the present application the parameters are functions of the stagger angle γ and of the axial interaction distance d between the blade mid-chord and the vane leading edges through the oblique wake length noted $x = d/\sin\gamma - c/2$. Model trends are required for τ and w_d as functions of x, and as functions of the blade loading, keeping in mind that a higher specific loading corresponds to a higher drag coefficient, thus a thicker wake. Indeed the various operating conditions of a tail-rotor are achieved by changing the stagger angle of the blades γ. Higher stagger angles correspond to deeper and sharper upwashs. For a preliminary assessment, empirical

wake models can be used [18,19]. Examples are plotted in Fig. 9-b for the extreme stagger angles $\gamma = 10°$ and $\gamma = 35°$ and an indicative value of the drag coefficient of the blades of 0.005. The uwpash is much more impulsive at the higher angle, which makes significant tonal noise expected. Comparing wake-interaction and potential-interaction in Fig. 9, the upwash is larger for the latter but less impulsive. This suggests that, because of the associated frequency content, potential-interaction noise contributes dominantly at low BPF harmonics whereas wake-interaction noise probably takes over at higher harmonics [20].

Typically as the wake-velocity profile is repeated in an infinite sum to generate the periodic signal of period $2\pi/\Omega$ corresponding to the heterogeneous rotor, the Fourier coefficients defined by

$$w(t) = \sum_{s=-\infty}^{\infty} w_s \, e^{i s\Omega t}, \qquad w_s = \frac{\Omega}{2\pi} \int_0^{2\pi/\Omega} w(t) \, e^{-i s\Omega t} \, dt$$

and referred to as the distortion harmonics are found as

$$w_s = w_d \frac{\Omega \tau}{2\pi} \sqrt{\frac{\xi}{\pi}} \, e^{-(s\Omega \tau)^2/(4\xi)} I_s.$$

They again involve the interference function of the rotor.

4.3. Calculation of the blade/vane loading harmonics

Though it can be not essential for the investigation of design-associated interference properties, the explicit calculation of the blade/vane loading harmonics is needed for quantitative noise estimates. This means that the unsteady lift distributed on the blades and vanes must now be determined from the velocity disturbances modeled in sections 4.1 and 4.2 for the potential-interaction noise of the rotor and the wake-interaction noise of the stator, respectively. In both cases closed-forms expressions derived from linearized unsteady-aerodynamic theories are available. They are shortly discussed below and re-conditioned for further use in near-field predictions and shroud-scattering computations.

Few analytical investigations are proposed in the literature for rotor potential-interaction noise. In the present work, the expression of the chordwise-distributed unsteady lift derived by Parry [21] and readdressed by Sanjosé et al. [22] is used. It is more representative of the actual aerodynamic conditions around the trailing edges of the blades than the one reported in Ref. [7]. Its two-dimensional character is relevant here because the blades and the shaft are both radial; this makes the interaction simultaneous all along a blade. However the present form of the solution assumes that the unsteady aerodynamic response at the blade trailing edge is the same as that of a semi-infinite plate, thus it ignores the leading-edge back-scattering. As a consequence the model is relevant for high frequencies. At lower frequencies a correction would be needed, not addressed in this paper. The expression reads

$$\ell_s(y_1) = A \, e^{i k_c (y_1^*-1)} \left[1 - \Phi(\sqrt{C}) \right] \tag{9}$$

introducing the non-dimensional chordwise coordinate $y_1^* = 2y_1/c$ with origin at the center chord, with

$$A = \frac{2i \rho_0 U w_s k_d}{\beta \sqrt{\mu^2 - K^2}}, \qquad C = i(\mu_s + K)(y_1^* - 1)$$

$$\mu_s = \frac{s\Omega c M_0}{2 \beta^2 U}, \qquad K = k_c + M_0 \mu_s, \qquad k_c = k_s + i k_d,$$

where k_d is a chordwise damping rate that accounts for the attenuation of the distortion upstream of the shaft. Φ denotes the complex error function with complex arguments [23]. $k_s = s\Omega/U$ is the hydrodynamic wavenumber and U the associated convection speed, here assimilated to the relative speed W on a rotor blade. The solution, Eq. (9) has been used in this section with approximate values of the damping rate k_d corresponding to the potential distortion around a circular cylinder, according to Ref. [6].

For stator wake-interaction noise, the aerodynamic response of the vanes to any distortion harmonic of the wakes is derived using the three-dimensional formulation of Amiet-Schwarzschild's theory, reviewed for instance in Refs. [24,25]. Three-dimensionality is a crucial need to correctly account for the effect of lean. Indeed the nearly-radial wakes issuing from the rotor in the tail-rotor case generate periodic loads that travel at some finite trace speed along the leading-edge of the leant vanes, as illustrated in Fig. 7. This trace speed U_t, function of ζ and of $\ell'(r)$, determines the radiation efficiency and is a key point of the low-noise design. More precisely, Amiet-Schwarschild's theory provides closed-form expressions of the lift for any Fourier component of oncoming disturbances called gust. A gust is characterized by two wavenumbers k_1 and k_2 in the chordwise and spanwise directions, y_1 and y_2 respectively. To reproduce the correct trace speed along the leading-edge of a vane segment, k_2 must be expressed as $k_1 U/U_t = \omega/U_t$, with $k_1 = \omega/U$, U being the convection speed of the disturbances, assimilated to the chordwise mean-flow speed relative to the considered vane segment or to the component V_r of the velocity triangle, and ω being the angular frequency of the excitation. The quantity $\tan^{-1}(k_2/k_1)$ is the skewness angle of the gust. Skewness acts in favor of the so-called sub-critical gusts, for which $k_2 > k_1 M/\beta$ if $M = U/c_0$ is the Mach number of the relative flow and $\beta = \sqrt{1 - M^2}$.
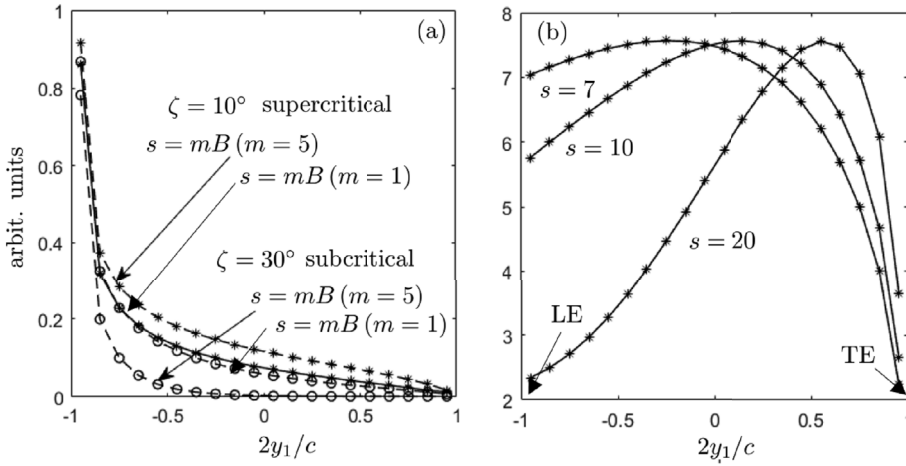
Fig. 11. Discretized amplitude distributions of the chordwise unsteady-lift (20 points for the illustration). (a): on the stator vanes for two BPF harmonics and sub-critical ($\circ$) and supercritical ($*$) conditions. (b): on the rotor blades for three harmonic orders s of the rotational frequency.

These gusts are known to radiate much less efficiently than the supercritical gusts, for which $k_2 < k_1 M/\beta$. A proper account of this effect is ensured by the present analysis. The explicit complex amplitude of the unsteady lift for a supercritical gust reads

$$\widetilde{\ell}(y_1, y_2) = \frac{2\,\rho_0\,U\,\widetilde{w}\,e^{i\pi/4}}{\sqrt{2\,\pi\,(k_1^* + \beta^2 \kappa)}}\,e^{i\,k_2^*\,y_2^*}\left\{1 - \sqrt{\frac{2}{1+y_1^*}} - (1-i)\,\mathrm{E}\left[2\,\kappa\,(1-y_1^*)\right]\right\}\,e^{-i\,(M\,\mu - \kappa)\,(1+y_1^*)}, \tag{10}$$

with $\kappa = \sqrt{\mu^2 - k_2^{*\,2}/\beta^2}$, $\mu = k_1^*/\beta^2$, $k_{1,2}^* = k_{1,2}c/2$ and $y_{1,2}^* = 2\,y_{1,2}/c$. E is the complex Fresnel integral introduced by Amiet

$$\mathrm{E}(\xi) = \int_0^\infty \frac{e^{i\,t}}{\sqrt{2\,\pi\,t}}\,\mathrm{d}t.$$

For sub-critical gusts κ is replaced by $i\kappa'$ with $\kappa' = \sqrt{(k_2^{*\,2}/\beta^2) - \mu^2}$ and the term $(1-i)\,\mathrm{E}\left[2\,\kappa\,(1-y_1^*)\right]$ by $\mathrm{erf}([2\,\kappa'\,(1-y_1^*)]^{1/2})$.

For simple far-field estimates in free field, Eqs. (9) and (10) can be used to generate closed-form expressions of the effective loading harmonics F_s, for instance from Eq. (2), because the chordwise integrals are derived analytically. But a numerical implementation is required for near-field predictions, such as those needed as input in a diffraction code. For this a blade/vane is discretized and the unsteady lift from Eqs. (9) and (10) is integrated analytically to provide expressions of the equivalent point dipoles on each rectangular mesh cell. The derivations are not reproduced here for conciseness but sample discretized 20-points chordwise distributions are shown in Fig. 11. The lift on a stator vane concentrates at the leading edge and goes to zero at the trailing edge by virtue of the Kutta condition included in the solution (Fig. 11-a). In the present case of 30°-lean the considered gusts are sub-critical: the lift increasingly concentrates at the very leading edges of the vanes as frequency increases. The same gusts are used for indicative computations at a less pronounced lean angle of 10°; they are now supercritical and more significant lift fluctuations are induced downstream of the leading edge. In comparison the unsteady lift induced on the rotor blades by the presence of the shaft spreads over the whole chord, essentially because the expected concentration at the trailing-edge is balanced by the effect of the Kutta condition. The lift is anyway higher in the aft part of the blades at sufficiently high frequencies. At low frequencies, here for $s = 7$ and $s = 10$, the high values at leading edge ($2y_1/c = -1$) are probably not realistic. A leading-edge correction, not implemented yet, should be included in Parry's model.

5. Free-field stator noise results

All formulae are given in the previous sections as a toolbox for early low-noise design of any subsonic architecture, in which potential-interaction noise and wake-impingement noise compete. Effects of lean, vane/blade number, stagger angle and uneven vane/blade spacing are then easily assessed by very fast and repeated calculations, well suited for integration in a genetic algorithm or any other optimization strategy. Yet the systematic application of all formulae and the investigation of all possibly varying parameters are well beyond the scope of the present paper. This is why the wake-interaction noise of the stator is selected in this section and later on to illustrate the methodology. Both a stator with a zero lean and a stator with the representative 30° lean angle are considered. More precisely the model with discretized vane-sources is implemented;
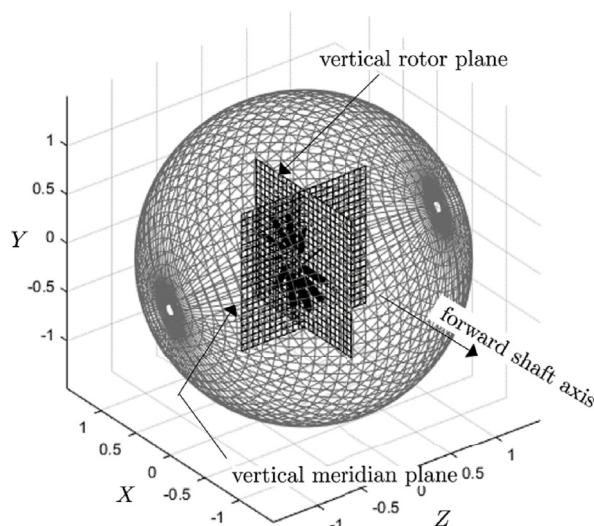
Fig. 12. Meshes used for acoustic extractions: vertical meridian plane of coordinates (Z, Y) $(X = 0)$, vertical plane of coordinates (X, Y) normal to the rotor axis $(Z = 0)$ and observation sphere. Stator vanes featured in the center part. Same coordinates as in Figs. 3-b and 4.

the radiation is calculated with the exact Green's function for the Helmholtz equation, so that the predictions are valid at all field points including the near field. Yet the far-field expressions may be used to interpret the modal structure of the radiated sound. In order to highlight the main effects of the design parameters, a reference stator with $V = 11$ equally spaced vanes has been considered, for comparison with the true stator shown in Fig. 4 with one vane removed because of the shaft. The vanes are considered as distributions of dipoles in the model according to Amiet's theory and the shaft is ignored. The rotor is made of $B = 10$ blades regularly spaced in the test: this only selects the BPF harmonics as the frequencies of interest.

The three-dimensional directivity is determined from an observation sphere of radius $R = 1.5$ m. The origin of coordinates is the center of the rotor disc at the mid-chord point of the blades (Fig. 3-b). This observation sphere and two scanning planes for further extraction of results are shown in Fig. 12. The stator is located downstream of the vertical rotor plane, at negative Z coordinates. A meridian vertical plane is also chosen. The lower part of both planes ($Y < 0$) is useful to investigate the directivity with the standpoint of an observer on the ground. Their size on the figure remains modest to be compatible with the computational domain defined in the numerical study of section 6. Though the verification is not detailed here, the features that will remain in the far field, such as the number and the angles of the directivity lobes and the dominant modes, are already established. Indeed the lowest considered Helmholtz number kR at the BPF for the 2920 rpm rotational speed is 13.5 on the sphere, ensuring at least the acoustic far-field condition. Yet slight variations could still be observed on the directivity pattern depending on the distance.

A typical map of the instantaneous acoustic pressure on the observation sphere is shown in Fig. 13 for the frequency 3BPF at 2920 rpm and a complete stator. The plotted quantity is the real part of the complex pressure calculated with the analytical model. Pairs of black and white traces indicate a period on the ϕ angle for a given value of the θ angle; they define a lobe of the corresponding mode and rotate with time as indicated by the arrows. A three-lobed counter-rotating pattern is seen around the axis (mode $n = -3$). Another eight-lobed co-rotating pattern (mode $n = +8$) covers a wide angular range on both sides of the rotor plane. Both are continuously connected to each other but separated by an extinction cone, the trace of which is marked by the dotted circle. For the present tests a vane has been split into five segments and each segment meshed with ten elements in both spanwise and chordwise directions.

Directivity patterns for the BPF as viewed from an oblique downstream angle are plotted in Fig. 14. The rotor axis is featured as the dash-dotted line and the schematic view of the incomplete stator from the same angle is added for clarity. Both the homogeneous stator with 11 vanes and the incomplete or heterogeneous stator with one vane removed are considered, at the slow and fast rotating speeds of 2920 rpm and 4500 rpm. In each case the gray meshed surface standing for the zero-lean configuration is transparent, so that the embedded black-meshed surface for the leant-vane configuration can be seen on the same plot. The radiation is nearly axisymmetric with no sound on axis in the homogeneous case, whereas the diagram is distorted in the case of the incomplete stator because the contribution of one vane is missing in the interference. At the low speed of 2920 rpm (Fig. 14-(a,b)), vane lean reduces the radiated sound without dramatical change in the overall shape of the directivity pattern. The apparent factor about 2 between the sizes of the gray and black surfaces makes a maximum sound reduction of 6 dB expected from the lean in this case. The directivity is imposed mainly by the modal structure. In the present test case at the BPF more sound is radiated at oblique downstream directions from axis, which results from the combination of the vane-to-vane phase shifts and of the vane angle. The dominant spinning mode produced by the interaction at the BPF
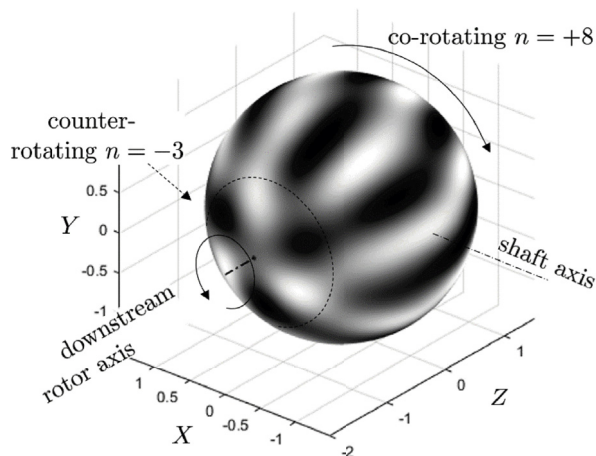
Fig. 13. Instantaneous pressure map on the observation sphere at 3BPF and 2920 rpm, featuring the dominant modal structure. Over- and under-pressures of the wavefronts as light and dark traces. Sphere radius 1.5 m.

is the mode -1 ($B - 11$ according to Tyler & Sofrin's rule, perfect with the homogeneous stator and moderately disturbed with the incomplete stator). Inversely, more sound would be radiated upstream were the same stator operating with a rotor of $B = 12$ blades, because of the dominant mode $+1$, not reported here. A direction of maximum radiation from axis is referred to here as a directivity lobe for convenience; it is a stationary notion, not to be confused with the spinning lobes defined as the angular periods of a radiation mode. When test predictions are made with the same parameters but at the higher rotational speed of 4500 rpm, the modal structure remains the same. Yet the effect of lean can differ, because for the same modes higher frequencies are involved, leading to different interference properties and a loss of compactness for sound radiation around the rotation plane. This is highlighted in Fig. 14-(c,d), where the downstream focused oblique emission of the mode -1, featuring a directivity lobe around 25° from axis, is more pronounced. Lean still performs well in reducing the sound emission of this lobe. However in directions close to the rotation plane, lean goes less effective and, for the heterogeneous stator (Fig. 14-d), either the zero-lean or the 30°-lean configuration is the loudest depending on the observation angle around the axis. The thick black lines in Fig. 14-(c,d) feature a cut of the directivity pattern in the vertical meridian plane for further examination in Fig. 18.

Sound directivity patterns at the higher frequency 3BPF are plotted in Figs. 15 and 16. The pattern for the complete stator in zero-lean configuration (Fig. 15) deviates from axisymmetry by 11 azimuthally-periodic lobes split into two sub-lobes. This is because the vane-to-vane distance $h = 2\pi r/11$ is no longer acoustically compact ($kh = 6.17$), whereas it was at the BPF ($kh = 2.06$). Two directivity lobes are also found in a meridian plane, featured by the thick black line in the figure, as a result of different interference properties between segments of a vane combined with the interference between vanes at a given radius. The configuration is the same as in Fig. 13. Therefore the narrow lobe pointing obliquely downstream at around 20° to the axis corresponds to the mode -3 ($3B - 3 \times 11$). The wider lobe radiating normal to the axis and seen as the large crown on the diagram corresponds to the higher-order mode $+8$ ($3B - 2 \times 11$). Many other modes contribute as expected from Eq. (4) but the modes -3 and $+8$ strongly dominate. The directivity pattern is only distorted without fundamental change when one vane is removed to reproduce the true heterogeneous stator.

The case of the 30°-leant vanes is reported in Fig. 16 with the same arbitrary amplitude scale as in Fig. 15. Again lean ensures an overall reduction of the radiated noise, with now different amplitude distributions between the main directivity lobes in the meridian plane. The most striking feature is that the radiated field of the heterogeneous stator exhibits a clear angular imbalance around the axis. Much less sound is radiated in the quadrant ($X < 0, Y < 0$), between the direction of the shaft corresponding to the forward-flight direction and the downward direction of the rotation plane, pointing to the ground. This relative extinction is associated with the missing vane, therefore its position depends on the lean angle and on the way the vanes are distributed with respect to the transmission shaft (see Fig. 4). More generally it could be observed or not depending on the configuration, therefore it is hard to rely on it for a general low-noise design rule.

Complementary tests at 3BPF and the higher speed of 4500 rpm are reported in Fig. 17 to emphasize differences with the same tone at lower speed. Four configurations, namely homogeneous and heterogeneous stators and zero and 30° lean angles, are considered. The overall sound level is nearly the same with radial and leant vanes as long as radiation normal to the axis is considered. Indeed the black-meshed and gray-meshed directivity diagrams interpenetrate. The only difference is that the dominant oblique directivity lobe in the meridian plane focusing upstream (positive values of Z) observed with radial vanes is strongly reduced with leant vanes. The absence of overall reduction around the rotation plane is again explained by non-compactness. At the higher considered frequency of 2.25 kHz the span is far from compact. The propagation-path differences between the sources are already large enough to induce cancellations, even for synchronous distributed sources along radial
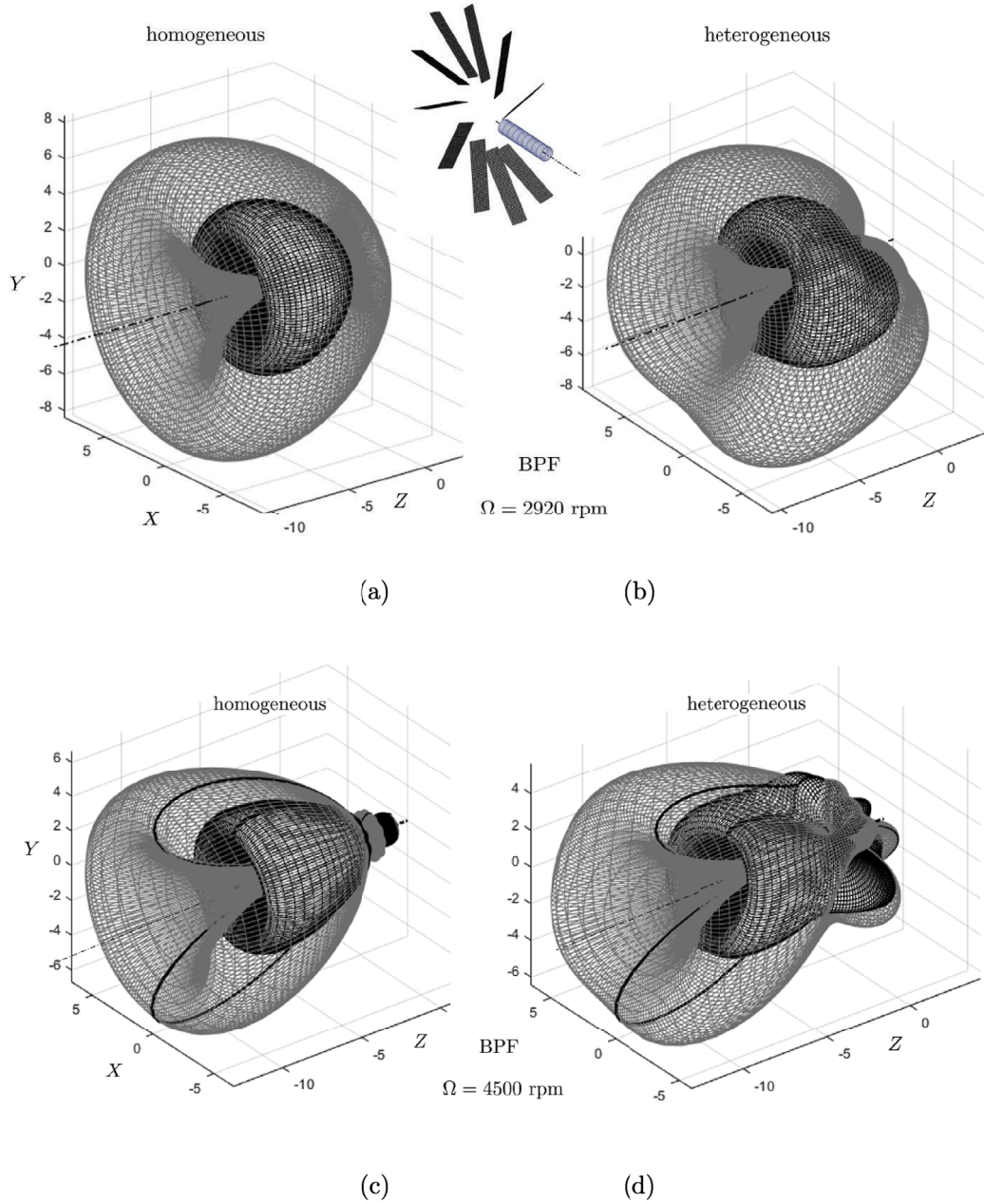
Fig. 14. Directivity patterns at the BPF for the homogeneous stator with $V = 11$ vanes (a–c) and for the heterogeneous stator with one vane removed (b–d). 2920 rpm (a–b) and 4500 rpm (c–d). Zero lean (transparent gray mesh) versus 30° lean (black inner mesh). Same arbitrary linear scale for all plots. Traces in the vertical meridian plane as thick black lines for plots in Fig. 18.

vanes, so that the benefit of lean is reduced. More precisely the Helmholtz number kL based on the vane span is around 3 at the BPF for 2920 rpm, and the one based on the tangential displacement due to lean about 1, corresponding to nearly compact source distributions for which lean induces additional (and beneficial) phase shifts. At 3BPF and 4500 rpm, kL is beyond 12.5; lean-induced phase shifts are of the same order of magnitude as the ones due to differences in propagation time. This suggests that lean is more effective in some low-to-medium frequency range, taking the spanwise Helmholtz number as reference.

A last and more quantitative illustration of the combined effects of lean and of stator heterogeneity is proposed in Fig. 18 where two-dimensional directivity diagrams in relative decibels are plotted in the (Z, Y) meridian plane, normal to the transmission shaft. Both the BPF at 4500 rpm and 3BPF at 2920 rpm are selected, reproducing the thick lines featured in Fig. 14(c and d), 15 and 16. Because the directivity is far from axisymmetric in the second case, different patterns would be observed in other
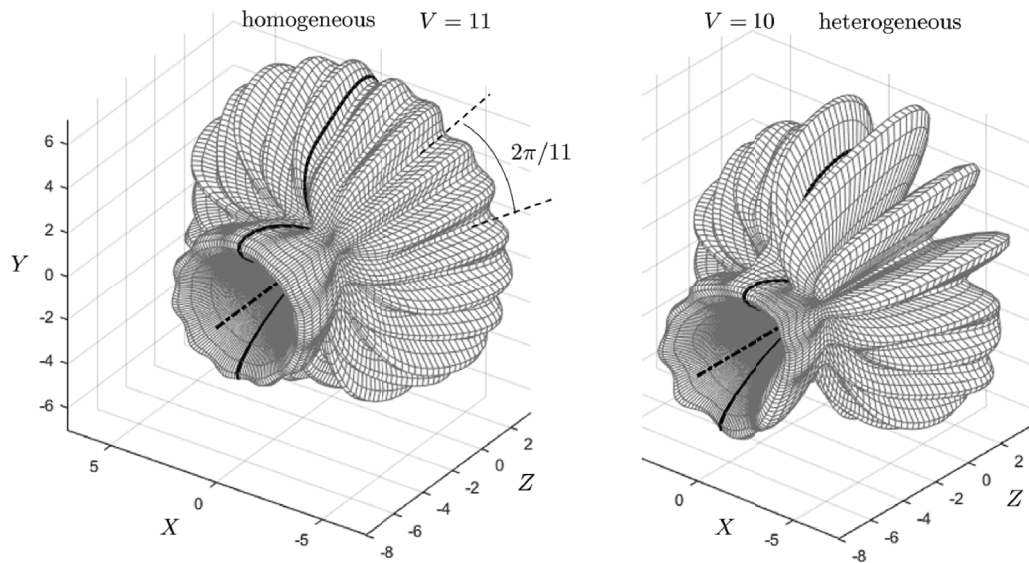
Fig. 15. Directivity patterns at 3BPF for the homogeneous stator with $V = 11$ vanes and for the heterogeneous stator with one vane removed. 2920 rpm. Zero lean. Same arbitrary linear scale as in Fig. 16. Traces in the vertical meridian plane as thick black lines for plots in Fig. 18.
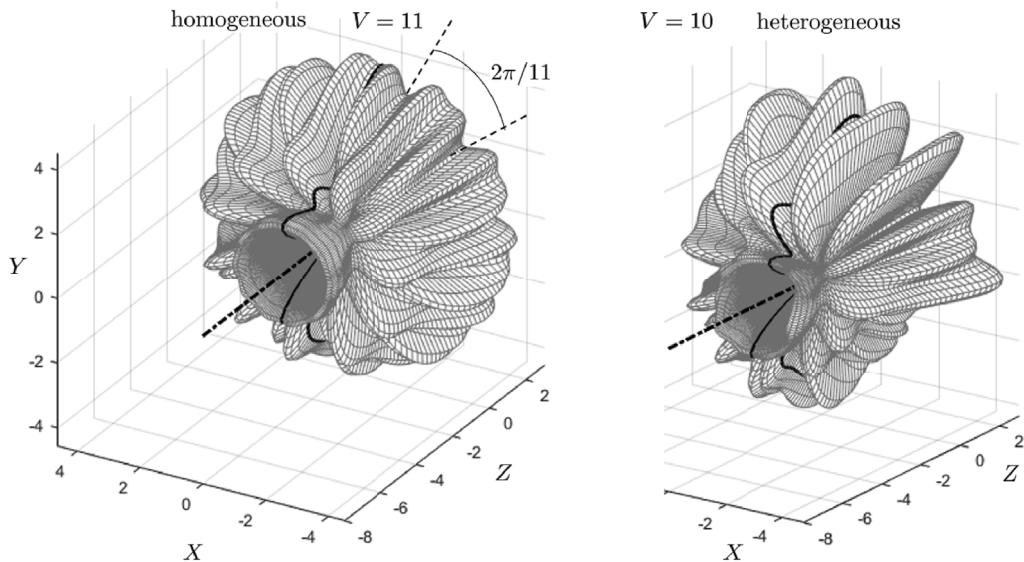

Fig. 16. Directivity patterns at 3BPF for the homogeneous stator with $V = 11$ vanes and for the heterogeneous stator with one vane removed. 2920 rpm. 30° lean. Same arbitrary linear scale as in Fig. 15. Traces in the vertical meridian plane as thick black lines for plots in Fig. 18.

meridian planes. Yet orders of magnitude of the lean-induced reduction are found by comparing either dashed or plain couples of thin-gray and thick-black lines. At the higher regime 4500 rpm and at the BPF, lean has the effect of reducing the downstream/upstream imbalance, with a reduction of the maximum directivity lobe by 5–6 dB; a small increase is found upstream where the sound was anyway already at low level. It is also worth noting that removing a vane from the purely periodic row of 11 vanes regenerates a substantial level of sound normal to the axis $\mathbf{e}_Z$. At the lower regime 2920 rpm and at 3BPF, lean reduces the oblique downstream lobe around 25° by again 5–6 dB. A significant reduction of about 5 dB is also found normal to the axis, with variations depending on the observation angle around the axis. These sample results confirm the substantial benefit of vane lean in the present configuration. But the various tests performed in this section stress the high sensitivity of the results with respect to any variation of all involved parameters. As a consequence, no general rule can be proposed without resorting to consistent model predictions.
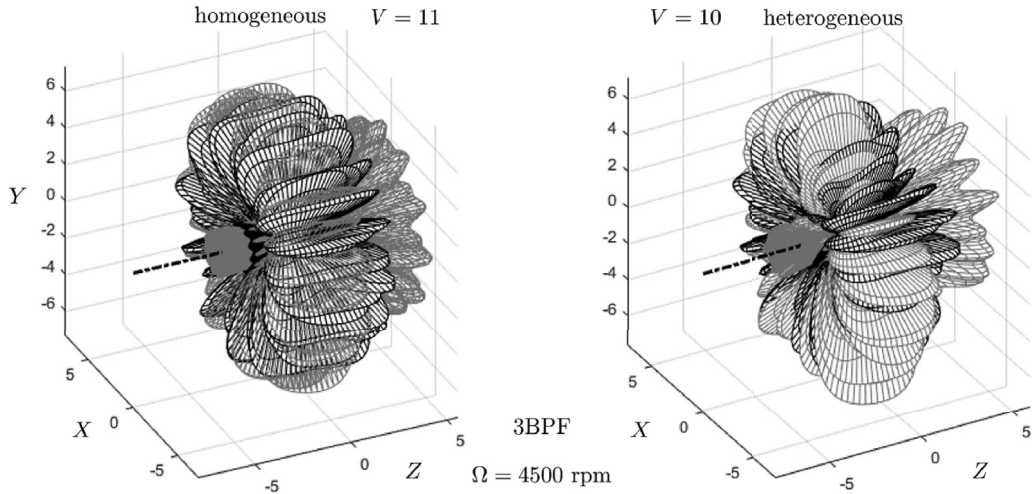
Fig. 17. Directivity patterns at 3BPF for the homogeneous stator with $V = 11$ vanes and for the heterogeneous stator with one vane removed. 4500 rpm. Zero-lean (gray) and 30° lean (black). Same arbitrary linear scale. Downstream axis as dashed-dot line.
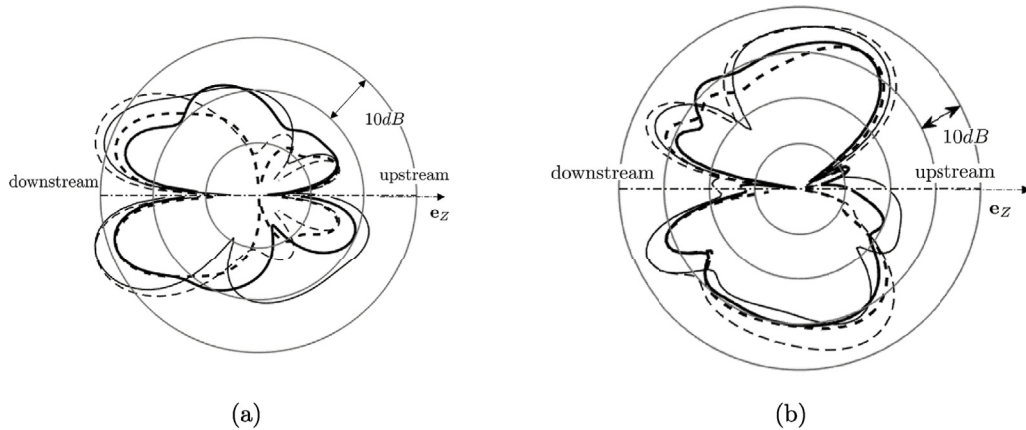

Fig. 18. Directivity diagrams in the (Z, Y) plane extracted from Fig. 14-(c,d) and from Figs. 15 and 16. (a): BPF at 4500 rpm; (b): 3BPF at 2920 rpm. Relative decibel scales. Zero lean (thin gray) versus 30° lean (thick black), homogeneous stator of 11 vanes (dashed) versus incomplete stator of 10 vanes (plain).

6. Scattering by the shroud

The presence of the casing might question some of the free-field results obtained in the previous section, at least from the point of view of noise assessment during the operation of a helicopter. It can be guessed that efficient modes mostly radiating in lateral directions are not a major issue for the environment, except if the helicopter is close to the ground. In contrast modes radiating in a vertical plane could be penalizing during overflight. But the casing acts as a screen for the latter and redistributes the radiated energy for the former. Its effects need to be quantified in various conditions for a proper understanding of the underlying mechanisms. The same need would be faced for the low-speed engine-cooling fans that are embedded close to obstacles of complicated geometry under the hood of a car, or for the installation of any fan in other engineering contexts. Therefore the problem of the sound radiation from modal sources in the presence of solid boundaries is of very general interest. Again the example of the shrouded tail-rotor must be considered here as a way of illustrating a methodology of much wider interest.

6.1. FEM software and numerical set-up

A simple geometry built with cylinders has been considered as casing test-case, shown in Fig. 19-a. The inner and outer radii of the outer part are $r_1 = r_T = 42$ cm and $r_2 = 52$ cm, and the constant thickness of the casing in the Z direction is $H = 20$ cm.
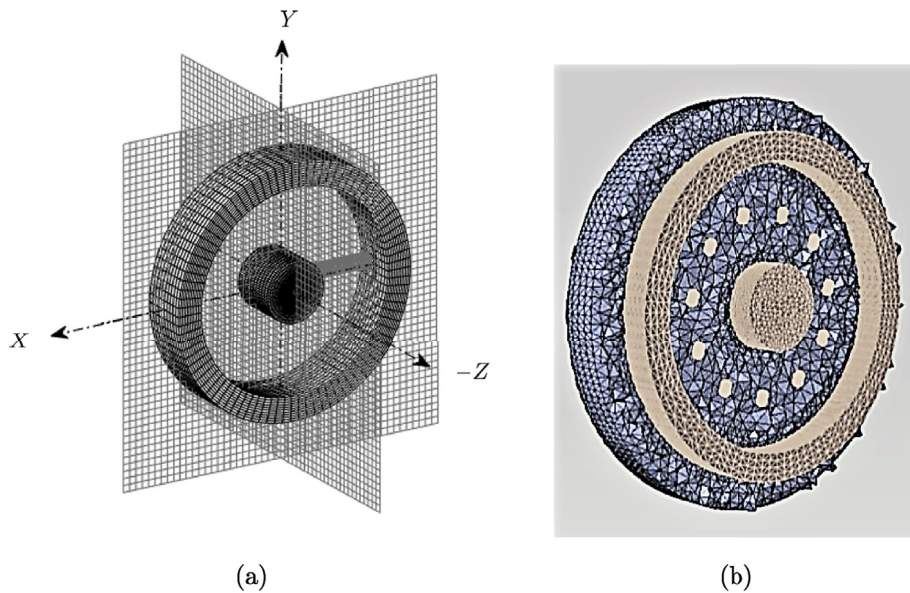
Fig. 19. Simplified shroud geometry and two main planes of numerical extractions (a) and detail of the actual FEM mesh structure with the circular array of 11 point sources (b). The transmission shaft is actually ignored in the computations.

The origin of coordinates is taken at the center point of the hub cylinder. As a result rotor-noise and stator-noise sources are located at positive and negative Z coordinates, respectively. Now acoustic installation effects caused by the shroud depend on size-to-wavelength ratios. The thickness of the casing H and to some extent the vane span are not far from compactness at the BPF for the regime 2920 rpm, whereas they are not for the higher BPF harmonics and/or for the higher regime 4500 rpm. This makes scattering occur in a range of parameters for which no approximate method is available. Therefore a Finite Element Method (FEM) is selected here, the principles of which are only outlined in this section. The FEM solves the Helmholtz equation via the discretization of a limited fluid domain. The latter is subjected to rigid-wall boundary conditions at the hub and shroud surfaces. Furthermore the Automatic Matching Layer (AML) property is used as radiating condition at the outer boundaries in order to let the acoustic field propagate outside without reflection back into the domain. Reflection and scattering from bodies of arbitrary geometry could be accounted for, so that the computations allow separating what comes from the intrinsic interference properties of the sources and what comes from the presence of the shroud. The computations are performed ignoring the flow, which is only valid as long as the axial Mach number remains small enough. The direct sound generated by any point dipole of complex strength $\mathbf{F}$ and angular frequency ω of the source distribution is needed to define both the direct sound and the incident pressure on the solid surfaces producing the scattered field. It is expressed as

$$p(\mathbf{x}) = -\mathrm{i}\,k\mathbf{F} \cdot \frac{\mathbf{R}}{R} \frac{\mathrm{e}^{\mathrm{i}\,kR}}{4\pi\,R} \left[1 + \frac{\mathrm{i}}{kR}\right]$$

where $R = |\mathbf{R}|$ is the propagation distance from a source and $k = \omega/c_0$ the acoustic wavenumber. The expression is uniformly valid. It accounts for near-field effects that are important when the distance from the source to the observer and/or the scattering body is not large when compared to the acoustic wavelength.

Again the WIN radiated by the stator is selected for the investigation of shroud scattering, in the continuation of the results discussed in the previous section. For this a complete set of 11 equally spaced stator vanes and an incomplete set with one vane missing are simulated in free-field and in the presence of hub and shroud. In principle source-modes of various radii should be included in the computations. Indeed sources located close to the blade or vane tips are expectedly the most efficient ones because they are characterized by higher relative flow speeds. They are also closer to the outer scattering surface of the casing and experience more pronounced masking than sources closer to the hub. The axial location of the sources also has an effect. Yet for simplicity of the present feasibility study, only point sources at the mid-span radius of each vane are considered in this section to allow a direct comparison with the analytically predicted free field. This already contains the basic interferential features of the modal structure and is enough to highlight the main effects. More extended computations could be performed by linear superposition in any application in engineering context. The 11 point dipoles of the complete stator configuration are featured in Fig. 19-b.

The FEM computations are performed on a laptop with 32 GB RAM and 4 cores of 2.90 GHz CPU power. The FEM mesh is made of 23 K nodes and 106 K TETRA4 elements. Based on the criterion of 6 elements per wavelength and using the element order 1 only, it would be valid up to 740 Hz in a conventional FEM solver. An adaptive order FEM (FEMAO) is used in the present work [26], carried out with the commercial software LMS Virtual.Lab [27]. The element orders are then automatically adapted by
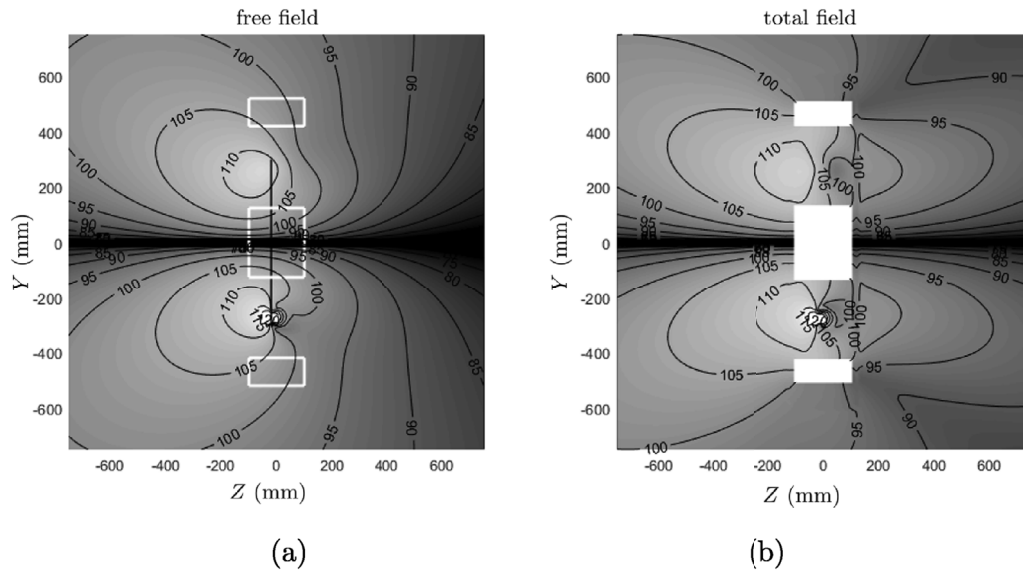
Fig. 20. Amplitude maps of the sound radiated at the BPF in the plane (Z, Y), with iso-contours in dB. Free-field (a) versus total field (b). Rotational speed 2920 rpm.

the solver based on the frequency of interest and on the source location (up to 10 with the current adaptation). For the highest frequencies, higher element orders are used with no need to re-mesh the computational domain, so that the same mesh can be used up to 15 kHz in the same solver. It is used here for the three investigated frequencies of 487 Hz, 973 Hz and 1460 Hz at 2920 rpm. The percentages of the volume of elements of order 1 are 100%, 98% and 40%, respectively. The remaining volumes correspond to the element order 2 in the present simulations. Fig. 19-b also shows a cut of the mesh of the acoustic domain. The computations are run in about 20 s for the first two frequencies and 35 s for the highest.

6.2. Sample results

Shroud scattering is primarily addressed in the (Z, Y) plane (see Fig. 19-a) corresponding to lateral sound radiation away from the flight path of a helicopter, at the BPF and its harmonic 3BPF. For this, acoustic-pressure level maps in free field and in the presence of the shroud are compared. The overall effect of the rigid boundaries in the surrounding of the sources is clearly visu-
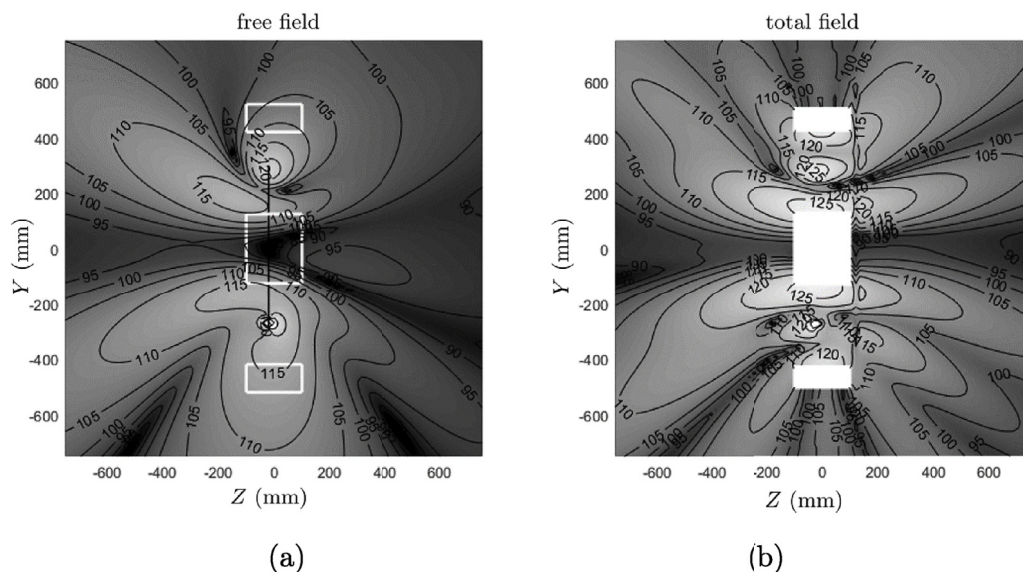

Fig. 21. Amplitude maps of the sound radiated at 3BPF in the plane (Z, Y), with iso-contours in dB. Free-field (a) versus total field (b). Rotational speed 2920 rpm.
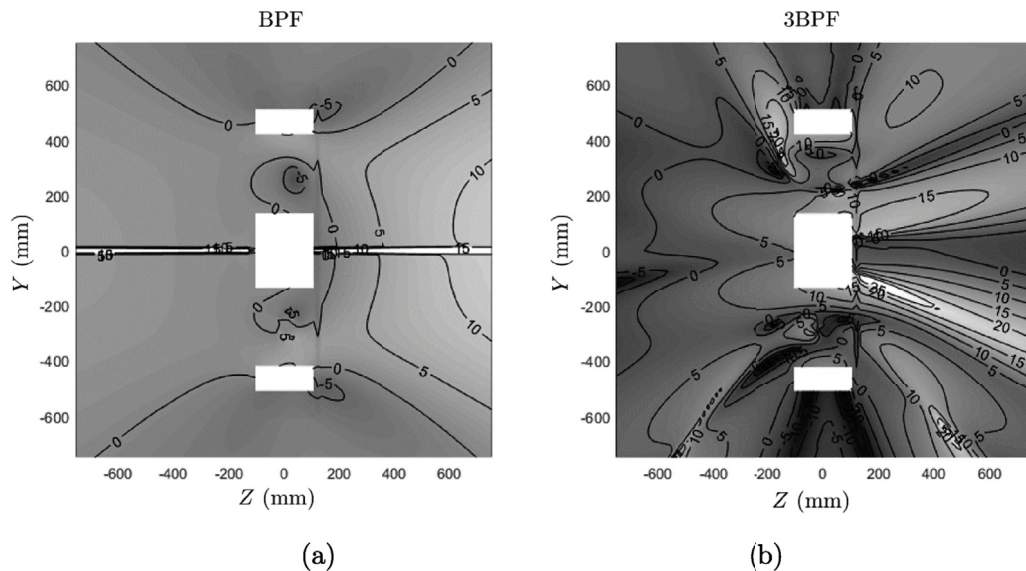
Fig. 22. Diffraction effect as produced by dB-difference of maps in Figs. 20 and 21, at the BPF (a) and 3BPF (b). Rotational speed 2920 rpm.

alized by keeping the same arbitrary color scale on both maps. The results are presented for the complete homogeneous stator but similar ones have been found for the 10-vaned stator, except for secondary field distortions that will be discussed later on. Results at the BPF are first shown in Fig. 20. The free-field is displayed in Fig. 20-a, where the position of the missing shroud is indicated by the white rectangles. The vertical black segment features the source circle. The total field is shown in Fig. 20-b, where the white areas stand for the presence of the shroud. The overall lobed structure in free field is nearly axisymmetric. It is obviously distorted when the effect of the shroud is taken into account. The main effect of the shroud is some tilting of the downstream lobe pointing around 45° to a smaller angle and the formation of a similar lobe upstream. Similar calculations performed for the 2BPF harmonic but not shown also exhibit radiation patterns close to axisymmetry, with significant modifications of the free-field directivity diagram only in the upstream range ±45° around the axis and small differences in other directions. For these first two tones at 2920 rpm the vane-to-vane distance remains compact.

In contrast the 3BPF harmonic involves clear non-compactness and the effect of the shroud and hub is more pronounced on it. The corresponding results, with the same conventions, are reported in Fig. 21. Shroud scattering now obviously redirects
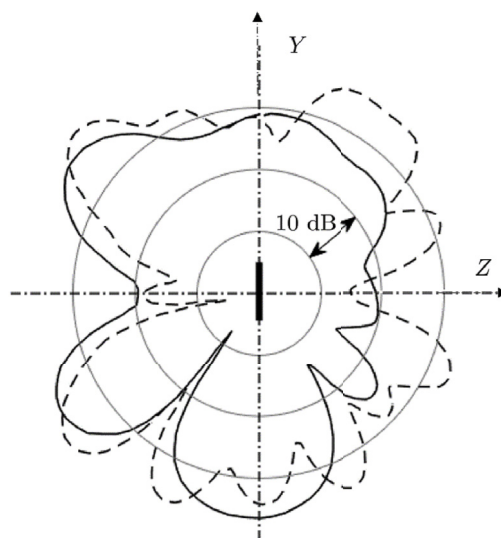

Fig. 23. Compared directivity diagrams in the (Z, Y) plane at a distance of 1 m for the tone at 3BPF, in free field (plain) and in the presence of the shroud (dashed). Incomplete stator of 10 vanes, rotational speed 2920 rpm.
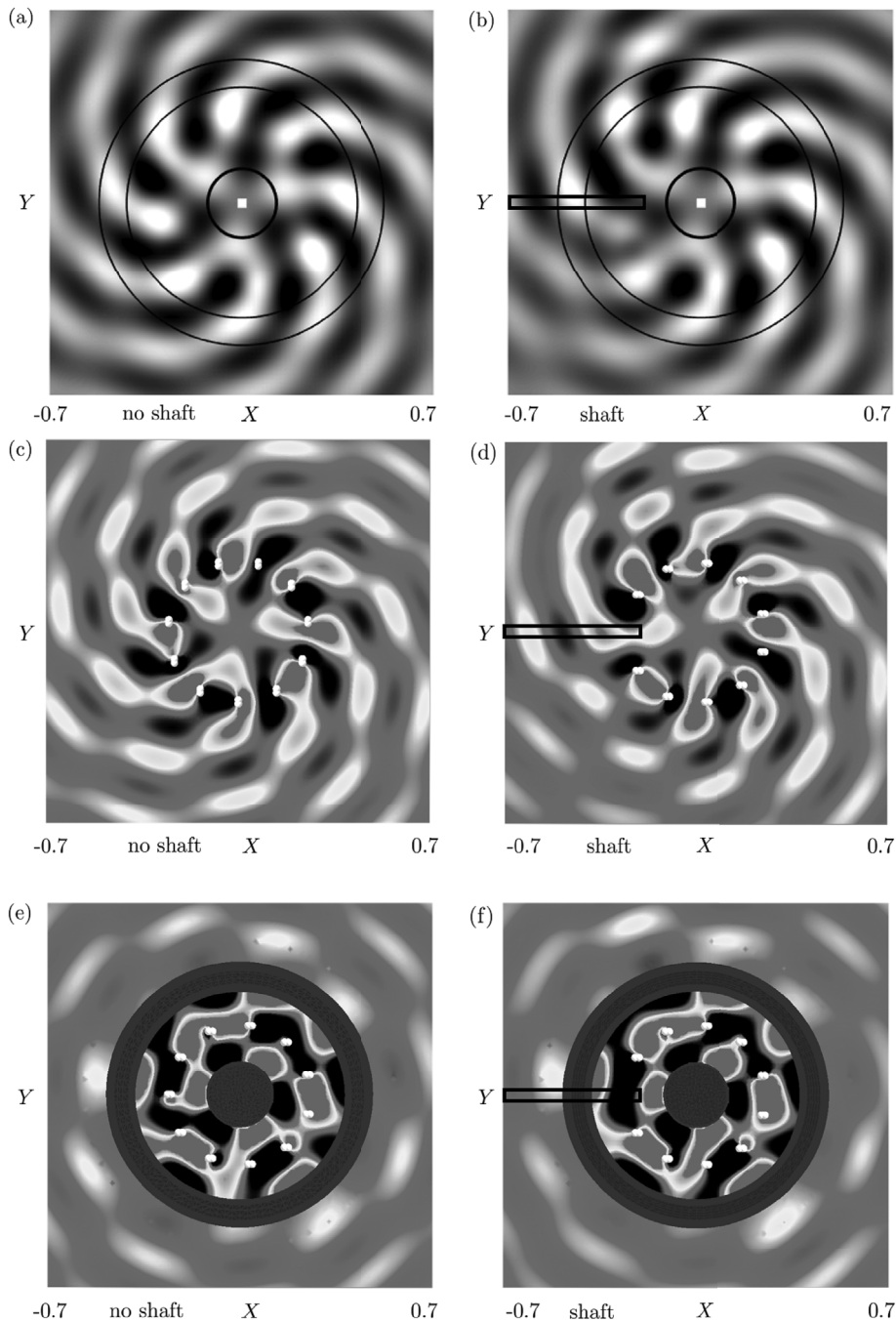
Fig. 24. Instantaneous acoustic-pressure maps at 3BPF and 2920 rpm in the (X, Y) plane, view from upstream. Left plots (a,c,e): complete homogeneous stator; right plots (b,d,f): incomplete stator. Upper plots (a,b): analytical free field; middle plots (c,d): numerical free field. Lower plots (e,f): numerical total field including shroud scattering. Position of the shaft indicated by the thin rectangle, white dots standing for the source positions in the numerical simulation.

radiation at oblique directions upstream (positive Z coordinate, right side of the map), resulting in a strong amplification around 15°–20° from axis. The wide free-field directivity lobe normal to the axis is also restructured by reflections on the casing and gives rise to additional extinction angles and lobes, clearly seen in Fig. 21-b. Some masking effect results, leading to a reduction of sound in a narrow angular range around the (X, Y) plane.

The amplification of the upstream radiation (inlet side of the tail rotor) appears as a common feature of all first three tones.

For a complete overview of typical acoustic features and a quantitative illustration of the scattering, the differences of the maps in Figs. 20 and 21 in terms of decibels are directly plotted in Fig. 22-a and -b for the BPF and 3BPF cases, respectively

(rotational speed 2920 rpm). The on-axis values for the BPF are meaningless because they result from differences of vanishing values. Except for a wide area of sound increase in the upstream quarter-space in the plane (Z, Y) that reduces the directivity imbalance shown in Fig. 20, the scattering amount is very weak. This indicates that there is no effective masking by the shroud for the BPF tone with regards to observers just below the helicopter. This behavior is typical of low frequencies for which the diffraction by the edges of the external part of the shroud regenerates sound in the shadow region. For this tone and apart from the lateral radiation, the purely analytical free-field model of the previous section is realistic. In contrast it is not anymore at the 3BPF harmonic. Indeed local amplification is found upstream around oblique angles, indicated by the light areas of the difference map in Fig. 22-b. Furthermore a significant masking is found below the shroud as emphasized by the dark area at the bottom of the map, which corresponds to observers below the helicopter in overflight.

The directivity diagrams in the (Z, Y)-plane 1 m away from the casing center-point and corresponding to the incomplete stator are plotted in Fig. 23. The plots confirm the partial shift of dominant radiation from downstream to upstream and the moderate but significant masking effect normal to axis. The masking is of about 5–6 dB around the negative Y direction. Sound radiation is not symmetric with respect to the Z-axis for two reasons. Firstly the non-compact vane-to-vane distance results in a polar directivity pattern around the axis with 11, thus an odd number of lobes as shown in Fig. 15. Secondly the incomplete array of vanes (10 instead of 11) disturbs the interference, which induces additional distortions.

It is worth noting that the masking effect by tail-rotor shrouds has been already found in previous theoretical diffraction studies as well as in experiments using an electronic spinning-mode synthesizer installed in a shroud mock-up [20]. It has also been recently addressed numerically by Guo [28].

For completeness the instantaneous-pressure maps finally shown in Fig. 24 illustrate the wavefront patterns at 3BPF and 2920 rpm in the (X, Y) plane normal to the axis. These patterns combine many spinning modes of radiation, some of which are characterized by the spiral wavefronts illustrated in Fig. 5. The analysis is performed for both the complete and the incomplete stators. The analytical prediction and the numerical simulation of the free field are compared in Fig. 24-a to -d. Keeping in mind that residual differences in the initial (constant) phase can remain and that the color scales can also slightly differ, the results are very similar, which validates both implementations. The acoustic free field obviously combines the expected mode -3, more apparent in the center area, and the mode $+8$ clearly identified in the outer region. Both are expected and were already highlighted on the view on the observation sphere in Fig. 13. The dominant directivity lobe of the mode -3 radiates at a small oblique angle from axis. In contrast the mode $+8$ dominantly radiates normal to axis. The simulated pressure fields in the presence of the shroud are presented in Fig. 24-e and f. The mode $+8$ is efficiently masked by the shroud, especially because the wavelength is of the same order of magnitude as the shroud width. This is why in the (Y, X) plane 8 spiral branches are observed in free field whereas only 3 reversed spiral branches are observed with the shroud. Shroud scattering has the effect of filtering the mode $+8$ for outside observers close to the rotation plane and confines its radiation inside. As a result, under the flight path of the helicopter the mode -3 now dominates the sound field at 3BPF whereas it should not in view of the free-field predictions. The results also clearly confirm in this case that the missing vane replaced by the shaft does not question the general features of the sound field; it only causes distortions on it. This could be different for other sets of parameters (vane number, frequency ...). The simple tools proposed in this work are precisely aimed at answering that question in a very fast way in any configuration of industrial interest.

7. Conclusion

At the early design stage of a rotor-stator system, only the global parameters and the main dimensions are known. Typically the flow rate and the pressure rise are already defined as targets. In contrast geometric details such as the precise shape of blade/vane cross-sections and the vane number can still be unspecified because they have to be optimized before producing the final design by resorting to specific algorithms. As a consequence the wake velocity deficit of a blade or the potential field around a vane cannot be accurately known either. Yet they are recognized as the only origin of the aerodynamic sound, at least at moderate Mach numbers. This means that noise can be predicted from a numerical resolution of fluid-dynamics equations only once the machine is completely defined. As a result acoustics cannot truly be accounted for in the optimization strategy. Analytical approaches are not facing the same stumbling block. They are based on a fundamental decoupling according to which the mean aerodynamic forces and the associated performances depend on the true blade/vane shapes, whereas the fluctuations around the mean forces do not. Now estimates of the latter are accessible analytically at the price of approximations of the aforementioned wakes and distortions, which means that acceptable acoustic predictions in terms of decibels are possible without precise information about the blade/vane design.

In this context the paper presented first a collection of formulas that can be used to model the free-field tonal noise radiated by a rotor-stator system with optional advanced design features such as uneven blade spacing and vane lean. The approach is in two steps. In the first step analytical models based on linearized unsteady aerodynamic theories are used to determine the lift fluctuations acting as sound sources. In the second step a simple radiation integral is derived. The formulas give access to the far-field radiation and its connection to basic interference properties of the sources, which is of primary interest for physical understanding and low-noise design. However for diffraction studies aimed at quantifying the effect of additional solid surfaces close to the rotor-stator stage, the direct near-field of the sources must also been reproduced. This is achieved analytically in this work by replacing the true sources by equivalent source-modes. The latter are discretized arrays of stationary and properly phase-shifted dipoles that can also be used as source terms in any numerical software solving the Helmholtz equation, typically FEM-based. They enable a uniformly valid field description in the entire space.

Precise applications are beyond the scope of the study, as well as an exhaustive investigation of all aspects that could be covered by the collection of formulas. For demonstrating the feasibility of the approach, various configurations of a shrouded helicopter tail-rotor have been selected as test cases and only the stator noise caused by equally-spaced impinging rotor wakes at harmonics of the BPF has been modeled. Coupling analytical source modeling with FEM computations provides fast and reliable estimates of the tonal noise, the order of magnitude of the computation time needed to produce a three-dimensional sound field at a single frequency being the minute. Comparing the free field with a numerically computed radiation in the presence of the shroud also allows understanding the basic contribution of the aerodynamic sources and its modification by diffraction. In the present work a simple, axisymmetric casing has been considered. This means that the spinning structure of the sound field produced by the sources is preserved and that only the spherical spreading that would take place in free field is affected by scattering. The results show that this modification is already significant; a true casing would induce even more pronounced changes because the spinning properties would be also modified. The minimum required input data in any more extended application would be the three-dimensional mean-flow velocity field, completed by an empirical wake model if needed. This can be provided by steady RANS (Reynolds-Averaged Navier-Stokes) simulations, which is believed quite accessible in engineering context. For preliminary design studies or noise impact assessment, the simplified models presented in the paper are believed a relevant alternative. The main conclusions for the advanced tail rotor can be listed as follows.

- Vane lean ensures substantial WIN reductions at relatively low-to-middle frequencies that correspond to Helmholtz numbers based on the span typically between 3 and 10. At higher frequencies the benefit of lean is partially lost. This is essentially a matter of rotational speed and BPF harmonic order. It is worth noting that lean is effective as long as the spanwise distributed sources have the same order of magnitude from hub to tip. It could lose interest if the sources concentrate too much at some radius.
- The modal structure of WIN is imposed by phase shifts between adjacent vanes. It remains the same either considering only one compact source on each vane or a complete source distribution over the non-compact vanes. Furthermore, at least with the present parameters, the same dominant modes are found for the incomplete stator with one vane missing (because replaced by the transmission shaft) and for a complete stator with equally spaced vanes. Replacing one vane by the shaft just results in a higher asymmetry of the directivity pattern. More crucial changes could probably be observed in another configuration.
- Shroud scattering is weak at low frequencies such as the BPF; in particular the masking effect of the shroud below the helicopter is negligible. In contrast a significant masking is predicted at the higher harmonic 3BPF, together with an increased lateral radiation upstream. This suggests that analytical free-field predictions are reliable at the BPF but that the diffraction by the shroud must be included in a second step at higher harmonics to produce realistic estimates.

References

[1] A. Vuillet, F. Morelli, New aerodynamic design of the fenestron for improved performance, in: 12th European Rotorcraft Forum, Garmish-Partenkirchen, 1986.
[2] J.E. Ffowcs Williams, D.L. Hawkings, Sound generation by turbulence and surfaces in arbitrary motion, Phil. Trans. R. Soc. A 264 (1969).
[3] J.E. Ffowcs Williams, D.L. Hawkings, Theory relating to the noise of rotating machinery, J. Sound Vib. 10 (1) (1969) 10–21.
[4] M.V. Lowson, J.B. Ollerhead, A theoretical study of helicopter rotor noise, J. Sound Vib. 9 (2) (1969) 197–222.
[5] D.L. Hawkings, M.V. Lowson, Theory of open supersonic rotor noise, J. Sound Vib. 36 (1) (1974) 1–20.
[6] M. Roger, Analytical modeling of the potential-interaction noise of a rotor due to a downstream rod, in: ISROMAC-14, Paper 34, Honolulu HA, 2012.
[7] M. Roger, S. Moreau, A. Guédel, Vortex-shedding noise and potential-interaction noise modeling by a reversed sears' problem, paper 2006-2607, in: 12th AIAA/CEAS Aeroacoustics Conference, Cambridge MA, 2006.
[8] M. Roger, P. Caule, Assessment of the effect of stator inhomogeneity on rotor-stator tonal noise, in: ISROMAC-15, Honolulu HA, 2014.
[9] M.E. Goldstein, Aeroacoustics, McGraw-Hill, NY, 1976.
[10] D.B. Hanson, D.J. Parzych, Theory for noise of propellers in angular inflow with parametric studies and experimental validation, NASA CR 4499 (1993).
[11] M. Roger, S. Moreau, Aero-acoustic installation effects in cooling fan systems, part I: scattering by surrounding surfaces, in: ISROMAC-12, Paper 2008-20222, Honolulu HA, 2008.
[12] M. Roger, Contrôle du bruit aérodynamique des machines tournantes axiales par modulation de pales, Acustica 80 (1994) 247–259.
[13] W. Dobrzynski, Propeller noise reduction by means of unsymmetrical blade-spacing, J. Sound Vib. 163 (1) (1993) 123–136.
[14] D. Ewald, A. Pavlovic, J.G. Bollinger, Noise reduction by applying modulation principles, JASA 49 (5–1) (1971) 1381–1385.
[15] P.E. Duncan, B. Dawson, Reduction of interaction tones from axial flow fans by suitable design of rotor configuration, J. Sound Vib. 33 (2) (1974) 143–154.
[16] E. Envia, M. Nallasamy, Design selection and analysis of a swept and leaned stator concept, J. Sound Vib. 228 (4) (1999) 793–836.
[17] J. de Laborderie, S. Moreau, Prediction of tonal ducted fan noise, J. Sound Vib. 372 (2016) 105–132.
[18] B. Reynolds, B. Lakshminarayana, A. Ravindranath, Characteristics of the near wake of a compressor or a fan rotor blade, AIAA J. 17 (9) (1979) 959–967.
[19] D.A. Philbrick, D.A. Topol, Development of a fan noise design system, part 1, in: 15th Aeroacoustics Conference, AIAA Paper 93-4415, Long Beach, CA, 1993.
[20] M. Roger, F. Fournier, An analysis of in-fin tail rotor noise, in: 12th European Rotorcraft Forum, Garmish-Partenkirchen, 1986, paper 40.
[21] A.B. Parry, Theoretical Prediction of Counter-rotating Propeller Noise, PhD. thesis, University of Leeds, 1988.
[22] M. Sanjosé, S. Moreau, M. Pestana, M. Roger, Effect of Outlet Guide Vane heterogeneity on the prediction of rotor-stator tonal noise, AIAA J. 55 (10) (2017) 3440–3457.

[23] M. Abramowitz, I.A. Stegun, Handbook of Mathematical Functions, Dover, NY, 1970.
[24] P.F. Mish, W.J. Devenport, An experimental investigation of unsteady surface pressure on an airfoil in turbulence, part 1: effects of mean loading, J. Sound Vib. 296 (3) (2006) 417–446.
[25] M. Roger, Broadband noise from lifting surfaces, analytical modeling and experimental validation, in: R. Camussi (Ed.), Noise Sources in Turbulent Shear Flows: Fundamentals and Applications, CISM Series 545, Springer, 2013, pp. 289–344.
[26] H. Beriot, A. Prinn, G. Gabard, Efficient implementation of high-order finite elements for Helmholtz problems, Int. J. Numer. Methods Eng. 00 (2014) 1–32.
[27] LMS Virtual.Lab 13.6 User Manual.
[28] N. Guo, Numerical prediction of the aerodynamic noise from the ducted tail rotor, Eng. Lett. 26 (1) (2018) 187–192.